The Astrophysical Journal, 696:1257–1277, 2009 May 10 doi:10.1088/0004-637X/696/2/1257

SPECTRAL STATES OF XTE J1701−462: LINK BETWEEN Z AND ATOLL SOURCES

Dacheng Lin, Ronald A. Remillard, and Jeroen Homan
Kavli Institute for Astrophysics and Space Research, Massachusetts Institute of Technology, 70 Vassar Street, Cambridge, MA 02139-4307, USA; lindc@mit.edu
Received 2008 September 19; accepted 2009 February 21; published 2009 April 23

ABSTRACT

We have analyzed 866 *Rossi X-ray Timing Explorer* observations of the 2006–2007 outburst of the accreting neutron star XTE J1701−462, during which the source evolves from super-Eddington luminosities to quiescence. The X-ray color evolution first resembles the Cyg X-2 subgroup of Z sources, with frequent excursions on the horizontal and normal branches (HB/NB). The source then decays and evolves to the Sco X-1 subgroup, with increasing focus on the flaring branch (FB) and the lower vertex of the "Z." Finally, the FB subsides, and the source transforms into an atoll source, with the lower vertex evolving to the atoll soft state. Spectral analyses suggest that the atoll stage is characterized by a constant inner disk radius, while the Z stages exhibit a luminosity-dependent expansion of the inner disk, which we interpret as effects related to the local Eddington limit. Contrary to the view that the mass accretion rate ($\dot{m}$) changes along the Z, we find that changes in $\dot{m}$ are instead responsible for the secular evolution of the Z and the subclasses. Motion along the Z branches appears to be caused by three different mechanisms that may operate at roughly constant $\dot{m}$. For the Sco X-1-like Z stage, we find that the FB is an instability track that proceeds off the lower vertex when the inner disk radius shrinks from the value set by the X-ray luminosity toward the value measured for the atoll soft state. Excursions up the NB occur when the apparent size of the boundary layer increases while the disk exhibits little change. The HB is associated with Comptonization of the disk emission. The Z branches for the Cyg X-2-like stage are more complicated, and their origin is unclear. Finally, our spectral results lead us to hypothesize that the lower and upper Z vertices correspond to a standard thin disk and a slim disk, respectively.

Key words: accretion, accretion disks – stars: individual (XTE J1701−462) – stars: neutron – X-rays: binaries – X-rays: bursts – X-rays: stars

Online-only material: color figures

1. INTRODUCTION

Based on their X-ray spectral and timing properties, the luminous and weakly magnetized neutron stars (NSs) in low-mass X-ray binaries (LMXBs) are classified into atoll and Z sources, named after the patterns that they trace out in X-ray color–color diagrams (CDs) or hardness–intensity diagrams (HIDs; Hasinger & van der Klis 1989; van der Klis 2006). Z sources typically radiate at luminosities close to Eddington luminosity ($L_{\rm EDD}$), and they trace out roughly Z-shaped tracks in CDs/HIDs within a few days. Atoll sources cover a lower and larger luminosity range (∼0.001–0.5 $L_{\rm EDD}$), and they trace out their patterns in CDs/HIDs on longer timescales (days to weeks). Although extensive coverage by the *Rossi X-ray Timing Explorer* (*RXTE*) has shown that atoll patterns can have Z-like shapes (Muno et al. 2002; Gierliński & Done 2002), they are different from the Z-source tracks in shape, color ranges, and evolution timescales. Furthermore, the spectra of Z sources are very soft on all three branches of the "Z," whereas the spectra of atoll sources are soft at high luminosities, but hard when they are faint. Properties such as the rapid X-ray variability and the order in which the branches are traced out, are also different for the two classes (Barret & Olive 2002; van Straaten et al. 2003; Reig et al. 2004; van der Klis 2006). The upper, diagonal, and lower branches of the Z-shaped tracks for Z sources are called horizontal, normal, and flaring branches (HB/NB/FB), respectively, while for atoll sources, they are called the extreme island, island, and banana states. To stay consistent with our previous work on atoll sources, however, we refer to the atoll branches as hard, transitional, and soft states (HS/TS/SS), respectively.

Based on the shape and orientation of their branches, the six classical Z sources were further divided into two subgroups (Kuulkers et al. 1994): Cyg-like (Cyg X-2, GX 340+0, and GX 5−1) and Sco-like (Sco X-1, GX 17+2, and GX 349+2). We show sample CDs and HIDs for these subgroups in Figure 1. The spectra from key positions along the "Z" are shown in Figure 2. We also plot the ratios of these spectra at the two ends of each branch (bottom panels) to show that the motion along each Z branch is the result of spectral changes in different energy ranges. The spectral differences between the two subgroups are quite apparent, especially in the case of the FB (red dot-dashed lines in Figure 2). Although the branches have the same names for each subgroup, their origins are possibly different. In addition to movement along the "Z" tracks, the Z tracks themselves display slow shifts and shape changes in CDs/HIDs. These so-called secular changes are most apparent in Cyg X-2.

There are several questions regarding the Z sources that remain unanswered: e.g., what is the nature of the Z branches, how do they relate to the spectral states of atoll sources, and how are the two Z subclasses related? A unique opportunity to improve our understanding of Z sources arose with the discovery in 2006 of XTE J1701−462 (Remillard et al. 2006), the first NS transient to show all the characteristics of a Z source (Homan et al. 2007c). In the first 10 weeks of its ∼600 day outburst, XTE J1701−462 transformed from a Cyg-like into a Sco-like Z source (Homan et al. 2007c), and during the decay it evolved further into an atoll source (Homan et al. 2007a). The upper and lower panels of Figure 3 show light curves of the outburst, using data from, respectively, the All-Sky Monitor (ASM; Levine et al. 1996) and the Proportional Counter Array (PCA; Bradt et al. 1993; Jahoda et al. 1996) on board

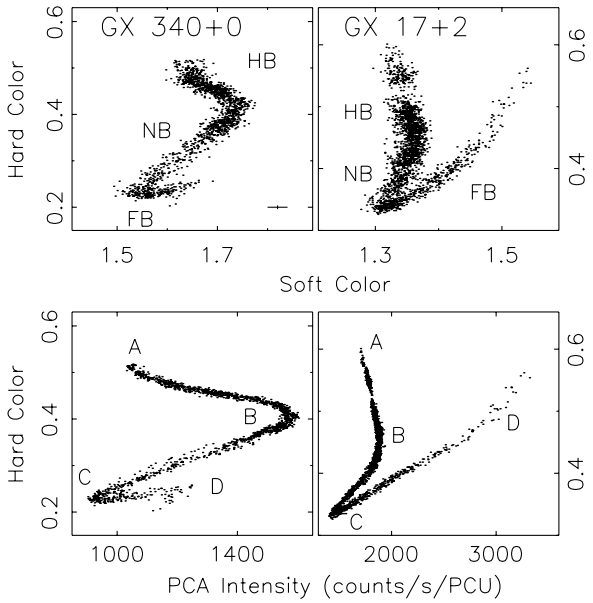

Figure 1. CDs and HIDs of the Cyg-like Z-source GX 340+0 (MJD 51920–51925) and the Sco-like Z-source GX 17+2 (MJD 51454–51464), with bin size 128 s. The typical error bars for the colors are shown in the top left panel; errors in the intensity are negligible. The Z-source branches (HB, NB, and FB) are labeled in the CDs. "A," "B," "C," and "D" in the HIDs mark key positions in the Z tracks: the left end of HB, HB/NB vertex, NB/FB vertex, and the right end of FB, respectively. Their corresponding spectra are shown in Figure 2.

RXTE. The latter one shows the luminosity as obtained from spectral fits (see Section 4 for more details). The two circles correspond to the peak luminosities of two type I X-ray bursts (persistent emission subtracted) which showed photospheric radius expansion (Lin et al. 2007a, 2009). In terms of a single value of Eddington limit (however, see Section 7), we see from this figure that the source reached super-Eddington luminosities during the peak of its outburst, assuming orbital inclination to be 70°.

The large dynamic range in luminosity of XTE J1701−462, from super-Eddington down to near-quiescence, also implies significant changes in the mass accretion rate ($\dot{m}$). This allows one to investigate the relevance of $\dot{m}$ to the questions that we posed above. The study by Homan et al. (2007c) suggests that differences in $\dot{m}$ are responsible for the Z-source subclasses, with the Cyg-like sources accreting at higher rates. Initial results from the end phase of the outburst suggest that the differences between Z and atoll sources are also purely the results of a difference in $\dot{m}$, with a lower $\dot{m}$ for the atoll class (Homan et al. 2007a).

Concerning the role of $\dot{m}$ in the evolution along the Z tracks, we note that results from multiwavelength campaigns have been interpreted as monotonically increases in $\dot{m}$ from the HB, through the NB, to the FB (e.g., Hasinger et al. 1990; Vrtilek et al. 1990). However, this classical view is inconsistent with the fact that the X-ray intensity decreases as Z sources move along the NB in the direction of the FB. In recent years, several alternatives have been proposed. Based on the behavior of the 0.1–200 keV flux as reported by Di Salvo et al. (2000) and on a comparison with black hole systems, Homan et al. (2002) suggested that $\dot{m}$ might be constant along the Z track, with motion along the "Z" being caused by an unknown parameter. Church et al. (2008) used X-ray spectral fits to claim that $\dot{m}$ increases in the direction opposite to the classical view, being lowest on the FB, which is a branch proposed to be driven by unstable nuclear burning. Finally, based on the observed change between Cyg-like and Sco-like Z-source behavior in the NS transient XTE J1701−462, Homan et al. (2007c) proposed that secular changes in Z sources are the result of changes in $\dot{m}$ and that the position along the "Z" is determined by $\dot{m}$ normalized by its long-term average. Definitive conclusions on the role of

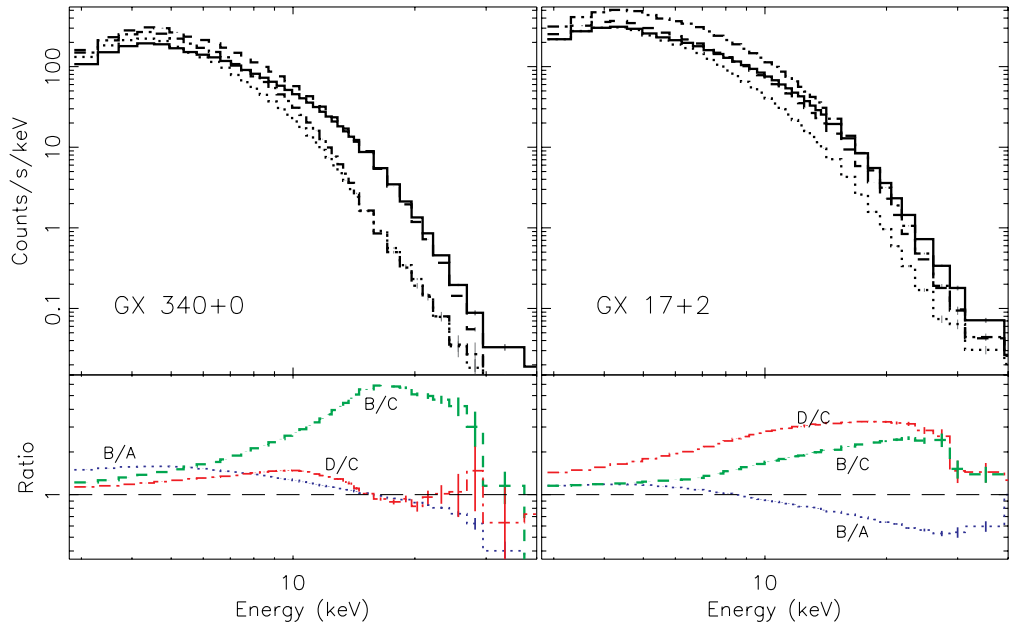

Figure 2. PCA spectra of GX 340+0 and GX 17+2 from key positions along their Z tracks. The solid, dashed, dotted, and dot-dashed lines correspond to labels "A"–"D" in Figure 1, respectively. The ratios of the spectra from the two ends of each branch are shown in the bottom panels. Spectra with high total PCA intensity are divided by those with lower total PCA intensity in order to show that on each branch the intensity increases in a different energy range.

(A color version of this figure is available in the online journal.)

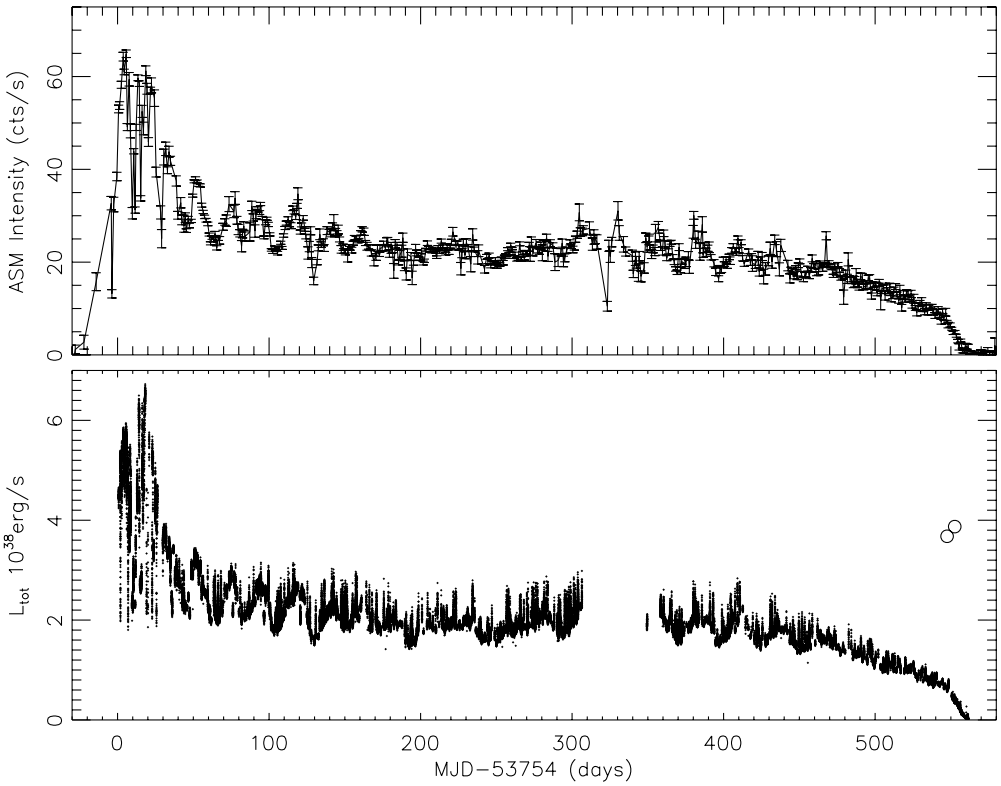

Figure 3. Upper panel: the *RXTE* ASM one-day-averaged light curve of XTE J1701−462 during its 2006–2007 outburst; lower panel: the *RXTE* PCA 32 s luminosity curve, from spectral fits with a MCD+BB model and assuming the source distance to be 8.8 kpc and system inclination 70° (Section 4). The two circles mark the peak luminosities (persistent emission subtracted) of two type I X-ray bursts, detected from this source during the decay of the outburst. These two bursts showed photospheric radius expansion, thus indicating the Eddington limit.

$\dot{m}$ have been hindered by the lack of a spectral model that lets us unambiguously track the evolution of physical components along the Z track.

A major difficulty in interpreting the X-ray spectra of NS LMXBs has been the problem of model degeneracy, i.e., significantly different models providing acceptable fits to the same data (Lin et al. 2007b, hereafter LRH07). In the classical framework of two-component models for the continuum spectra of NS LMXBs, one component is thermal, and the other is Comptonized. The thermal component can be either a single-temperature blackbody (BB), used to describe the boundary layer, or a multicolor disk blackbody (MCD), while there are choices for the nature of the Comptonized component, with no clear advantages for any set of combination of these two components. As far as Z sources are concerned, Done et al. (2002), Agrawal & Sreekumar (2003), and D'Aí et al. (2007) used a model of Comptonization plus an MCD to fit the spectra of Cyg X-2, GX 349+2, and Sco X-1, respectively, while Di Salvo et al. (2000, 2001, 2002) used a model of Comptonization plus a BB for GX 17+2, GX 349+2, and Cyg X-2. The model used by Church et al. (2008) for their study of GX 340+0 also consisted of a BB plus Comptonization, with the latter approximated by a cutoff power law.

In LRH07, we showed for two atoll-type transients that the commonly used spectral models for thermal emission plus Comptonization are not favored for the SS, because they fail to satisfy various desirability criteria, such as $L_X \propto T^4$ evolution for the MCD component and similarity to black holes for correlated timing/spectral behavior. In an attempt to solve this, we devised a hybrid model: a BB to describe the boundary layer plus a broken power law (BPL) for the HS, and two strong thermal components (MCD and BB) plus a constrained BPL (when needed) for the SS. The results from this model are summarized as follows: both the MCD and BB evolve as $L_X \propto T^4$, the spectral/timing correlations of these NSs are aligned with the properties of accreting black holes, and the visible BB emission area is very small but roughly constant over a wide range of L_X that spans both the HS and SS. We note that this model is still partially empirical, especially the (constrained) BPL description of Comptonization. We also note that the boundary layer spectrum was reported to be broader than a BB in the Z-source HB and atoll-source SS (Gilfanov et al. 2003; Revnivtsev & Gilfanov 2006). However, it is also possible that the broadening is caused by rapid variability of a Comptonized component and its blending with a BB in these states/branches.

Considering the success of this spectral model for atoll sources, we intend to apply it to XTE J1701−462. This unique source was observed on an almost daily basis with *RXTE* during its outburst. In this work, we present a color/spectral analysis of all *RXTE* observations from the 2006–2007 outburst of XTE J1701−462, as part of our campaign to understand this source (Lin et al. 2009: type I X-ray bursts; J. Homan et al. 2009, in preparation: transition from a Z to an atoll source; J. Fridriksson et al. 2009, in preparation: quiescence). The goal of this paper is to improve our understanding of the physical processes that drive the evolution along the Z-source tracks and the link between the Z-source branches and atoll-source states. A description of our data set and reduction techniques is given in Section 2. In Section 3, we present an analysis of the CDs/HIDs. States and branches are classified for the entire outburst, and we study the global evolution of the Z/atoll tracks. Using our state/

branch classification, in Section 4 we present our spectral fit results as a function of increasing source luminosity. Each of the Z-source branches and transitions between them (i.e., the vertices) is examined in terms of repeatable patterns in the evolution of spectral parameters. Results of a brief investigation of timing properties are presented in Section 5. In Section 6, we present a physical interpretation of the evolution of the source and some of the branches and vertices of the Z track, and we discuss the role of $\dot{m}$. A comparison with other NS LMXBs is also given. Finally, we summarize our main conclusions in Section 7.

2. OBSERVATIONS AND DATA REDUCTION

We analyzed all 866 pointed observations (∼3 Ms) of XTE J1701−462 from the 2006–2007 outburst made with the PCA and the High-Energy X-ray Timing Experiment (HEXTE; Rothschild et al. 1998) instruments. For the PCA we only used data from Proportional Counter Unit (PCU) 2, which is the best-calibrated unit. For the HEXTE only Cluster B data were used, because all the observations of this outburst were made after 2006 January, when Cluster A started experiencing frequent problems with rocking between the source and background positions. We used the same standard criteria to filter the data as described in LRH07. Only observations with PCA intensity (background subtracted) larger than 10 counts s^{-1} PCU^{-1} were considered. Appropriate faint/bright background models were used when the source had intensity lower/higher than 40 counts s^{-1} PCU^{-1}. Deadtime corrections for PCA and HEXTE data were also applied.

To spectrally model the evolution of the source during the entire outburst, we must create pulse-height spectra on an appropriate timescale. This timescale should be short enough to characterize the spectral evolution, but also long enough to minimize statistical uncertainties. XTE J1701−462 showed rapid spectral variations on some occasions, especially on the FB. To characterize these variations, we created spectra with exposures of 32 s and 960 s, from "standard 2" data of PCU 2. The 960 s spectra were created by combining 30 sequential 32 s spectra with a maximum observational gap <500 s. Although we allow several gaps in a 960 s spectrum, in the end all such spectra have time span <1600 s. Longer observation gaps than 500 s limit the exposure to <960 s. If a spectrum had an exposure <320 s, it was combined with the preceding spectrum if the time gap between them was <500 s; otherwise it was omitted. The final selection of spectra for modeling was based on our understanding of the source variability, using the 32 s and 960 s spectra (see Section 3.4.1).

Once we had spectra from the PCA for spectral modeling, we created the response file for each spectrum using HEAsoft version 6.4. An investigation of Crab Nebula observations revealed that the low-energy channels still showed calibration issues after 2006. Therefore, we used channels 4–50 (numbering from 1 to 129; ∼2.7–23.0 keV) for our spectral fitting and applied systematic errors of 0.8% for channels 5–39 (below 18 keV) and 2% for channels 4 and 40–50. We created the HEXTE spectra to match the PCA spectra in observation time. No systematic errors were applied for HEXTE data.

The observations of XTE J1701−462 were contaminated with a small amount of diffuse Galactic emission within the large field of view of the PCA (∼1°; J. Fridriksson et al. 2009, in preparation). Count rates near the end of the outburst, between Modified Julian Day (MJD) 54321 and 54342, reached a constant level, ∼2 counts s^{-1} PCU^{-1} (after the normal background subtraction), due to this diffuse component. The next *RXTE* pointed observation of this source was nearly five months later and indicated a similar level of residual flux. To correct for the diffuse emission, we created a spectrum from the observations between MJD 54321 and 54342 and applied it as an extra background correction. We only did this for observations between MJD 54300 and 54321, when the source intensity was <300 counts s^{-1} PCU^{-1} and the diffuse emission could skew the spectral results significantly.

In order to study the source evolution in a model-independent manner, we also examined the CDs/HIDs of XTE J1701−462. We calculated X-ray colors as described in LRH07. We normalized the raw count rates from PCU 2 using observations of the Crab Nebula, and we defined soft and hard colors as the ratios of the normalized background-subtracted count rates in the (3.6–5.0)/(2.2–3.6) keV bands and the (8.6–18.0)/(5.0–8.6) keV bands, respectively. Throughout the paper, all PCA intensity values are normalized and correspond to the sum count rate of these four energy bands. The difference between the normalized intensity and the raw total PCA count rate is normally <5%.

3. LIGHT CURVES AND COLOR–COLOR DIAGRAMS

3.1. Source State/Branch Classification

Normalized light curves, CDs, and HIDs of the outburst of XTE J1701−462 are shown in Figures 4 and 5. The two light curves in Figure 4 have bin size 32 s, and they show count rates from the 2.2–3.6 and 8.6–18.0 keV energy bands, respectively. They are quite different, with the high-energy curve showing rapid and strong flaring, and the low-energy curve showing a ∼25 day modulation (Homan et al. 2007c) that varies in strength with time. The CDs and HIDs in Figure 5 were made from 960 s spectra to minimize the statistical uncertainties. The entire outburst is divided into five time stages, denoted by Roman numerals I–V. Their boundaries are marked by vertical dot-dashed lines in Figure 4, and the CDs and HIDs corresponding to each of the stages can be found in Figure 5. The boundaries between the stages are somewhat arbitrary, but are based on the following considerations: (I/II, MJD 53783) the source switches from Cyg-like to Sco-like Z-source behavior in the CD, as reported in Homan et al. (2007c); (II/III, MJD 53929) the long-term modulations at low energies become weaker and slower; (III/IV, MJD 54232) the long-term modulations disappear, and the final decay starts; (IV/V, MJD 54303) the flaring at high energies ends.

Most of the observations in stages I–II were analyzed in detail by Homan et al. (2007c) and shown to exhibit Z-source characteristics. Stage I is characteristic of a Cyg-like Z source, and stages II–III are similar to the Sco-like Z sources (Figure 5). In stage IV, the source is similar to some of the bright atoll sources, such as GX 9+1 and GX 9+9 (Homan et al. 2007b). While in those sources the observed flaring would be referred to as an upper banana branch, our analysis (see below) shows that it is simply a lower luminosity version of the FB. In our view, the flaring is one of the defining characteristics that separate the Sco-like Z sources from the atoll sources. Thus, we group stage IV with stages I–III and refer to them as the Z (source) stages. In stage V, XTE J1701−462 showed characteristics of an atoll source (Homan et al. 2007a), and we will refer to this stage as the atoll (source) stage. Finally, we note that the secular changes in stages II and III are mainly the result of the long-term modulations.

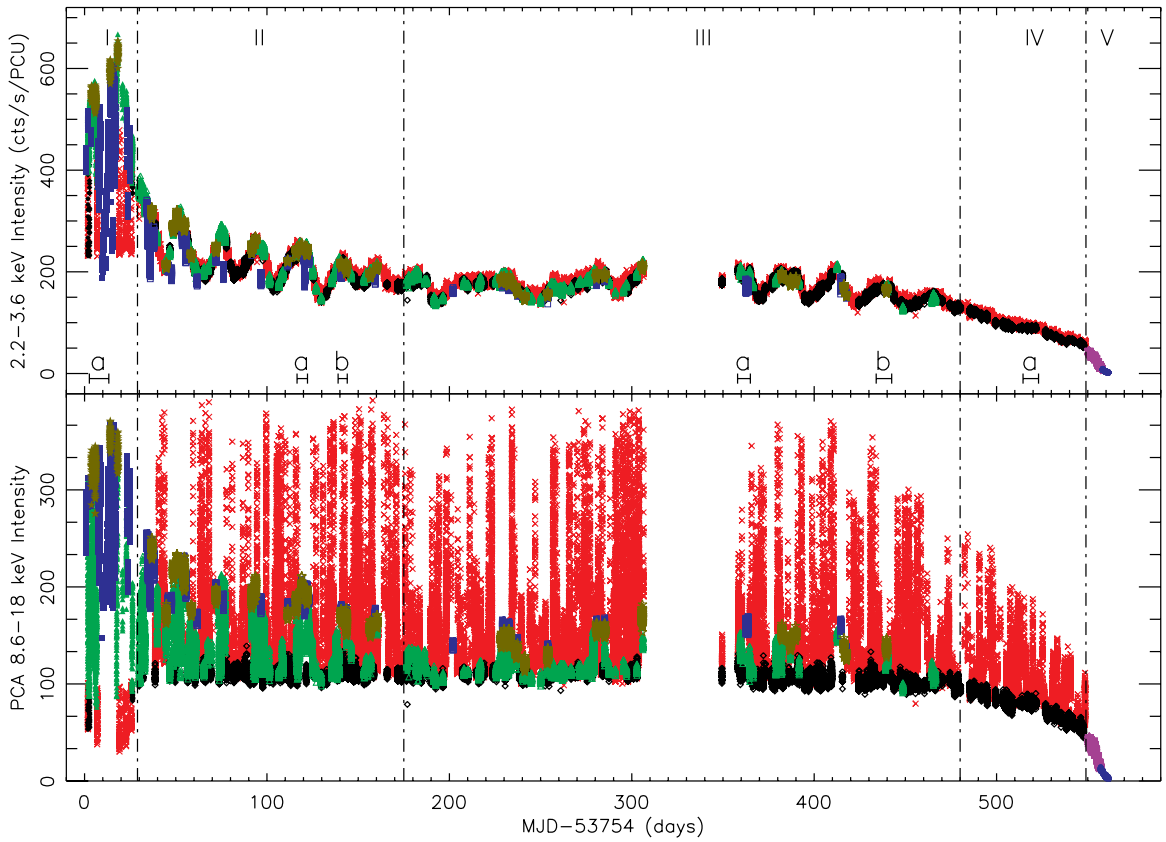

Figure 4. *RXTE* PCA 32 s light curves of XTE J1701−462 in two energy bands during the 2006–2007 outburst. The typical error bars are smaller than the symbol size. The outburst is divided into five stages. In stages I–IV, the source showed characteristics of Z source, with the HB, NB, and FB marked by blue squares, green triangles, and red crosses, respectively. We also mark the HB/NB and the NB/FB vertices by olive pentagrams and black diamonds, respectively (Figure 6). In stage V, the source showed characteristics of atoll source, with the HS and SS marked by blue filled circles and purple hexagrams, respectively. The "a" and "b" in each stage mark the sample intervals for which detailed source properties are shown in Sections 3.4.2 and 4.3.

An important step toward understanding the evolution of the source is the classification of the observations in terms of states and branches. For sources showing substantial secular changes, this is normally done by dividing the data sets into smaller subsets, in order to identify clear tracks in the CDs/HIDs (e.g., Wijnands et al. 1997; Homan et al. 2007c). The observations of XTE J1701−462 are not long and dense enough (typically one hour per day) to do this for the entire data set, as the secular changes often smear the Z tracks before they are completely covered. A different way of classification is therefore necessary. Fortunately, we can take advantage of the fact that each branch shows systematic evolution in the CDs/HIDs of each of the stages. The HID for the entire outburst is shown in Figure 6; the position of the Z vertices throughout the outburst is marked by the solid and dashed lines, and the plot symbols that we use to differentiate the states/branches are given for reference (see below). We note that clear vertex lines are still seen if we define colors using the different energy bands that were used in Homan et al. (2007c).

The atoll stage V is divided into the HS (blue filled circle, with HC $>$ 0.55) and SS (purple hexagram). Since little short-time variation is seen in stage V, each data point in Figure 5 corresponds to one entire PCA observation, and we also combine several observations when the source intensity is $<$30 counts s^{-1} PCU^{-1}. These same data intervals for stage V are used for spectral analysis in Section 4.

The branch classification strategy for Z stages proceeds as follows. Stages II–IV are Sco-like, and we focus on them first. In these stages, the HB, NB, FB, HB/NB vertex, and NB/FB vertex are marked by (open) blue square, green triangle, red cross, olive pentagram, and black diamond symbols, respectively (Figure 6). We made a preliminary branch classification in the CDs by hand, using data in $\sim$10 day time intervals, and found that the NB/FB vertex always hovers near the bottom of the corresponding HID. During the outburst, the motion of this vertex is described well by a single line (i.e., the solid line) in the HID of Figure 6. Data below this line are identified as NB/FB vertex in stages II–IV. This line is also shown in the HIDs of stages I and V in Figure 5 for reference. The FB in stages II–IV is most easily identified in the CDs; it can be separated from other branches by simple lines (solid lines in the CDs of Figure 5 for stages II–III), while excluding the NB/FB vertex points described above. In stage IV, the HB and NB are absent, and the FB consists of all the points that remain after the NB/FB vertex points are identified.

For stages II and III, the HB, NB, and HB/NB vertex classifications still need to be defined. We first manually identified HB/NB vertex points based on the CDs and HIDs for a few short intervals ($\sim$10 days). Again, we found that they lie near a single line in the HIDs, i.e., the dashed line in Figure 6. This dashed line is also shown for reference in the HIDs of Figure 5. We identify the observations with a HC value within 0.01 of this line as the HB/NB vertex, excluding those on the FB, which were identified earlier. The other observations above and below this line were identified as the HB and NB, respectively. At this point, the branch classification for Sco-like

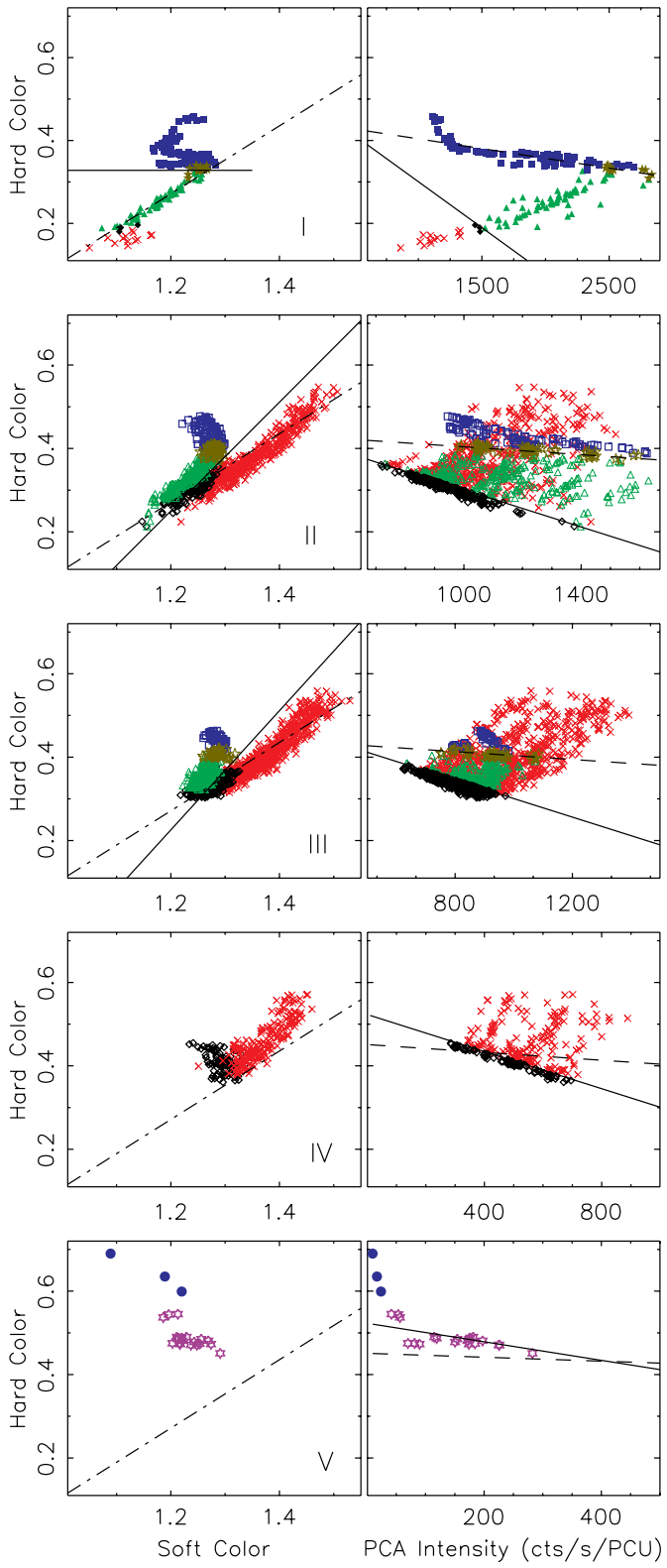

Figure 5. CDs and HIDs for the five stages of the outburst defined in Figure 4. The bin size is ∼960 s for stages I–IV, while for stage V each data point corresponds either to one PCA observation or several observations combined (when the count rates are less than 30 counts s^{-1} PCU^{-1}). The meaning of the symbols are the same as in Figures 4 and 6. The solid and dashed lines are used to define the source branches. The typical error bars are smaller than the symbol size. The dot-dashed line is aligned with the NB in the CD of stage I and is shown in other panels of CDs for reference.

Table 1
Statistics for Observation Time of the Source in Different States/Branches

	Observation Time in ks and (Percentage of the Total)				
Source State/Branch	I	II	III	IV	V
HB	96 (55)	90 (9)	40 (3)	0 (0)	...
HB/NB vertex	10 (6)	42 (4)	33 (3)	0 (0)	...
NB	52 (31)	228 (24)	178 (14)	0 (0)	...
NB/FB vertex	2 (1)	201 (21)	291 (24)	77 (33)	...
FB	12 (7)	408 (42)	687 (56)	156 (67)	...
SS	...	...	...	...	54 (58)
HS	...	...	...	...	40 (42)

Z stages II–IV is complete. The classification process can be summarized as follows: the NB/FB vertex is identified by a line near the bottom of HIDs, the FB is separated from other branches in the CDs, and the HB/NB vertex lies around a single line in the HIDs, above and below which are the HB and NB, respectively (excluding the FB and NB/FB vertex).

Cyg-like stage I spans about one month and mainly consists of two tracks. It shows strong dips (lower panel in Figure 4). The solid line which limits the NB/FB vertex in stages II–IV in the HIDs also applies to this stage (Figure 5), with the "dipping" FB falling below the line, rather than above it. The boundary between the HB and NB is defined by a constant HC line in the CD. The HB/NB vertex points for the two main tracks are identified by hand. They fall close to the extension of the vertex line found for stages II–IV, as shown in Figure 6 (dashed line). The HB, NB, FB, HB/NB vertex, and NB/FB vertex in this stage are marked by (filled) blue square, green triangle, red cross, olive pentagram, and black diamond symbols, respectively (Figure 6).

3.2. Source Evolution and Relations Between Source Types

With the classification of the source states/branches in place, we now investigate the global evolution of XTE J1701−462 during this outburst. Table 1 gives a summary of the amount of time that the source is observed in the different branches/states of each stage. Although these values are somewhat dependent on the definition of the boundaries between the source states/branches, it is quite clear that the fractions of time that the source stays on the HB and NB decrease with the evolution of the outburst with that on the HB decreasing faster. The source stays on the NB/FB vertex and the FB more and more frequently from stage I to stage IV. Moreover, while the source spends most of the time (greater than 90%) on the HB and NB in stage I, it is not observed on the HB and NB at all in stage IV. We note that during each stage, the source often moves back and forth along the NB or the FB without entering another branch (Figure 4). Although there are no discontinuous jumps from one branch to another, the source often reverses its direction within a branch. We do not see a clear constraint as to when a source enters a specific branch, which seems to be random. The only exception is the occurrence of the HB during stages II and III, which appears mostly, but not exclusively, around the peaks of the long-term modulation as observed in the low-energy light curve (Figure 4).

Following the disappearance of the HB and NB during stage IV, the FB disappears in stage V, and the original NB/FB vertex smoothly evolves into an atoll track. This is reflected both in the light curves (Figure 4) and in the HID (Figure 6). Moreover, there is no observational evidence that suggests that

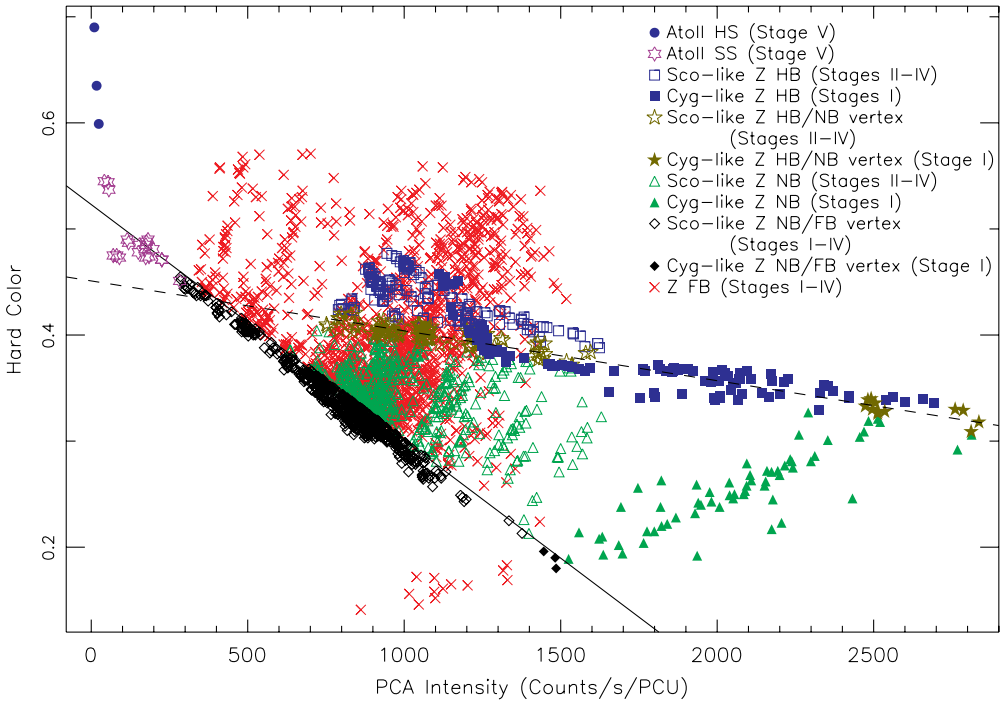

Figure 6. Complete HID of the outburst of XTE J1701−462. For reference, a legend of all different symbols is shown in the upper right corner; they apply to all other figures in this paper.

the HB evolves into the atoll SS or the atoll HS as $\dot{m}$ decreases (Muno et al. 2002; Gierliński & Done 2002; Homan et al. 2007c). Another interesting phenomenon seen in Figure 6 is that the distance between the HB/NB vertex and the NB/FB vertex in the HID decreases with intensity (or equivalently, the NB shortens as the intensity decreases). In the HID, the HB/NB vertex line crosses that of the NB/FB vertex near the point where the FB disappears and the atoll track starts.

The Cyg-like HB/NB and NB/FB vertices seem to be natural extensions of Sco-like ones at high intensity (Figure 6). The Cyg-like NB also resembles the Sco-like ones. However, there are clear differences between the Cyg-like dipping FB and Sco-like strong FB. The HB in the Cyg-like stage is also very distinctive. It spans a much larger range of intensity than in other stages (Figure 6). However, in contrast with the FB, whose pointing direction switches from downward to upward in the HID as soon as the source enters stage II, the HB seems to transit more slowly, as it is still nearly horizontal and has significant range of intensity in stage II, especially at high intensity (Figure 5). This can be seen more clearly from sample intervals in Section 3.4.2. The HB becomes vertical only when the intensity is ∼800–1300 counts s^{-1} PCU^{-1} (Figure 6). It is interesting to see in Figure 6 that the nearly horizontal part of the Cyg-like HB (excluding the upturn) is closely aligned with the line traced out by the HB/NB vertex. This might hint at some connection between that part of the Cyg-like HB and the HB/NB vertex in the Sco-like Z stages. The upturn of the HB of the Cyg-like stage happens to have an intensity similar to the Sco-like HB. Considering that they are both vertical in the HID, they might be related, which we investigate based on spectral and timing properties later in this work.

3.3. Evolution Speed Along Branches

Clues regarding the physical origin of each Z branch might be reflected in the timescales on which the source evolves along it. We therefore measure the speed at which XTE J1701−462 moves along its Z track. Such speed measurements have been made in the past for other Z sources (e.g., Wijnands et al. 1997; Homan et al. 2002). These authors used a rank number to track the source position along the Z track, which is scaled to the full length of the NB. This is very difficult to implement for XTE J1701−462, as it shows large secular changes of the tracks in the CDs/HIDs, making it hard to universally assign a rank number for all tracks. Instead, we measure the speed for each branch separately, by choosing a quantity X that changes substantially and is suitable for tracing the position along that branch. The normalized position in that branch can then be expressed as $S = (X - X_{\rm min})/(X_{\rm max} - X_{\rm min})$, where the maximum ($X_{\rm max}$) and minimum ($X_{\rm min}$) values are obtained in a time-dependent manner. When sequential data points have position numbers S_i and S_{i+1} and centroid temporal separation Δt, the speed at position $(S_i + S_{i+1})/2$ is calculated as $|S_{i+1} - S_i|/\Delta t$. This method is hereafter referred to as the rank-shift method. Using the normalized position in a branch, we also calculate a second measure of evolution speed, which is the inverse value of the fraction of the time that the source spends at each position of the branch. This method is valid under the assumption that our sampling does not bias the results.

For the FB and the NB/FB vertex, our speed measurement utilizes the intensity in the energy band 8.6–18.0 keV, since it shows strong changes (Figure 4). The source moves very fast along the FB, and 32 s spectra are used. We find that the intensity in this band maintains nearly constant minimum (∼100 counts s^{-1} PCU^{-1}) and maximum levels (∼350 counts s^{-1} PCU^{-1}) during stages II–III. Thus, we set $X_{\rm min} = 100$ counts s^{-1} PCU^{-1} and $X_{\rm max} = 350$ counts s^{-1} PCU^{-1} for stages II–III. For stage IV, the range of the intensity at 8.6–18.0 keV on the FB changes with time. Thus, we divide stage IV into intervals of 20 days and dynamically define $X_{\rm min}$ and $X_{\rm max}$ for each interval. Stage I has few FB observations, which are all dipping; they are not investigated.

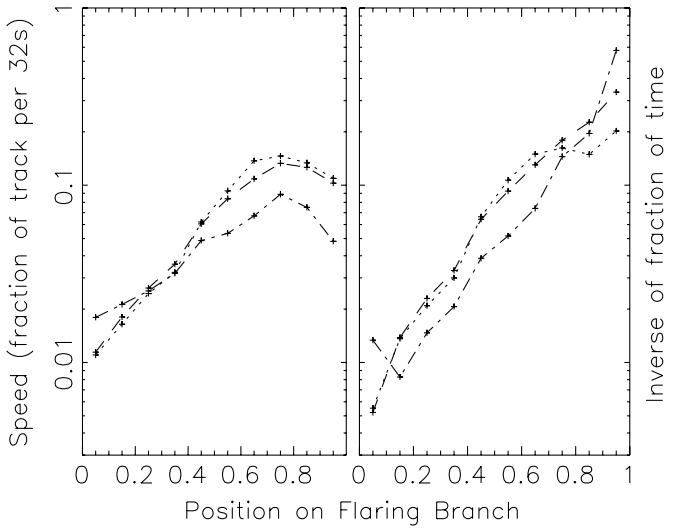

Figure 7. Left panel: the speed of the source along the FB, expressed as the average fraction of the FB track that the source goes through in 32 s. The FB is normalized to have length one, with the NB/FB vertex set to be 0.0. The position on the FB is based on the 8.6–18.0 keV intensity. The statistical error is very small, but the sample standard deviation is about as large as the speed itself. Right panel: inverse of the fraction of time in each segment (the normalization is arbitrary). This quantity is an alternative measure of the speed of the source along the FB (Section 3.3).

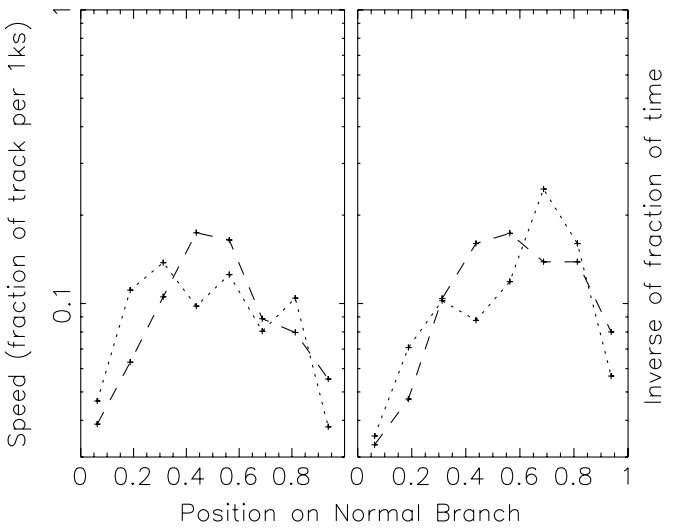

Figure 8. Same as Figure 7 but for the NB. The NB/FB vertex has a position value of 0.0, and the HB/NB vertex is 1.0. Time bins of 960 s are used for this plot.

The rank-shift results for the FB are shown in the left panel of Figure 7, using dotted, dashed, and dot-dashed lines for stages II, III, and IV, respectively. The NB/FB vertex has position number 0.0. We average the speed for ten bins along the FB. The statistical errors are very small, but the sample standard deviations per bin have values of order the speed. It is clear that the speed increases by about an order of magnitude as the source ascends the FB. The plot shows a slight decrease in speed at the tip of the FB, but this may be an artifact of the source reversing its direction at this position; if the speed at the top of the FB is high, this can occur within the timescale of our 32 s measurements. Based on the measured speed, we estimate that it takes ∼10 minutes for XTE J1701−462 to cross the FB in one direction. The right panel of Figure 7 is the inverse of the fraction of the time that XTE J1701−462 spends at each position of the FB. This result resembles the rank-shift method, in support of our finding that the speed increases as XTE J1701−462 ascends the FB.

The situation for the NB is more complicated. Figure 4 suggests that the intensity at 8.6–18.0 keV is also a good tracer for the position along the NB; the NB is much more pronounced here than in the low-energy band. Samples of the NB show that it takes much longer time, about several hours, for XTE J1701−462 to travel across the NB. Hence, we use 960 s spectra to reduce the effect of short-time fluctuations. We only select intervals with complete tracks of the NB, i.e., including both the HB/NB and NB/FB vertices. Only stages II and III are considered, since only these two stages provide sufficient data. The results are shown in Figure 8. Because of its shorter range, the NB is divided into eight bins. Again we show the rank-shift method on the left and the method of the inverse fraction of time on the right. The NB/FB and HB/NB vertices have position numbers 0.0 and 1.0, respectively. Both stages and both methods give a common result: the speeds at the HB/NB and NB/FB vertices are much smaller than in the middle of the NB. Based on the speed measured here, we estimate that it takes about 3 hr for the source to cross the NB (excluding the first and last bins, assumed to be occupied by the vertices). The NB and FB branch crossing times have been independently confirmed from light curves and CDs/HIDs.

It is harder to measure the speed along the HB. Data samples (Section 3.4.2) show that it takes ∼1 day for the source to trace out the HB, a timescale at which the secular changes of Z tracks become significant. The intensity decreases at high energy, but increases at low energy as the source climbs up the HB from the HB/NB vertex (Section 3.4.2). This suggests that a broad hardness ratio such as (2.2–3.6 keV)/(8.6–18.0 keV) can be an effective means to track the source position on the HB. However, even this quantity only changes by at most 20% in stages II–III. Moreover, the end point of the HB is not well defined, which impedes our efforts to measure the evolution speed along the HB.

In summary, for the Sco-like Z branches it takes ∼10 minutes, ∼3 hr, and ∼1 day for the source to go through the FB, NB, and HB, respectively. The NB/FB vertex appears to represent a point of increased stability, compared to the adjoining branches, since the source evolves much slower when it enters this vertex. Figure 8 shows that the source slows down as it enters the HB/NB vertex from the NB, but we do not know whether the evolution speeds up as the source leaves the HB/NB vertex along the HB. Figures 7 and 8 can be interpreted to suggest that the FB and NB are unstable configurations relative to their ending vertices. We cannot say much about the Cyg-like Z stage I, due to insufficient observations, but a few samples also shows that the source moves much slower on the HB than on the NB or FB.

3.4. Selection of Spectra for Spectral Fits

In this section, we examine the variability of XTE J1701−462 in different energy bands. The variability results will guide the data selection for our spectral fits, to be conducted over the entire outburst. We also investigate in detail the properties of a few sample intervals that exhibit evolution along Z branches. These samples will also be used later for our spectral analysis, to help us understand the physical causes of evolution along each branch.

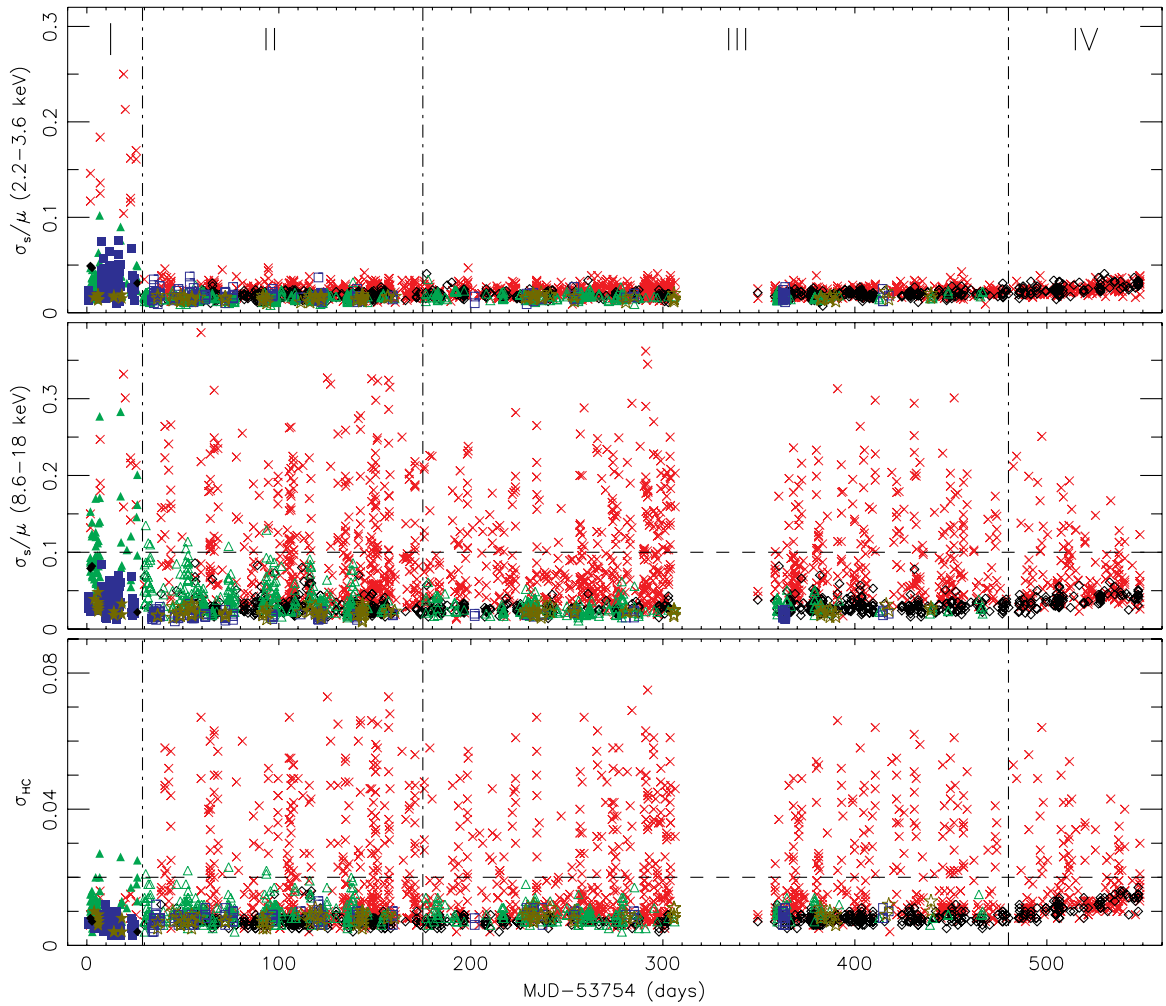

Figure 9. Different measures of spectral variability during the Z stages. Each point corresponds to one 960 s spectrum. The top two panels show the fraction of variability in two energy bands, using quanta of 32 s spectra for each point. The bottom panel is the corresponding sample standard deviation of the hard color.
(A color version of this figure is available in the online journal.)

3.4.1. Variability in Different Energy Bands

The spectra in the atoll stage V show little variation within a typical PCA observation (Figure 4), and the spectrum of complete observations can be used for spectral fitting. However, variations are more significant and faster during the Z stages I–IV. We quantify the variations of the spectra within the time span of each 960 s spectrum using the 32 s spectra that it contains (see Section 2). We calculate the sample standard deviations (σ_s) and the means (μ) of the source intensity in the low- and high-energy bands and plot the fraction of variability (σ_s/μ) in Figure 9. In the low-energy band, the intensity varies little (∼2%) within ∼960 s in all branches, except for stage I where it varies up to ∼25% on the dipping FB.

In the high-energy band, the source intensity on the FB can vary up to 30% within ∼960 s, while the HB and the NB typically show <10% variability. Also plotted in Figure 9 is the sample standard deviation of the hard color ($\sigma_{\rm HC}$), again using the quanta of 32 s spectra within a given 960 s spectrum. Its variability is similar to the source intensity at high energy: $\sigma_{\rm HC}$ is <0.02 (∼4%) except on the FB where it can be up to 0.08 (∼15%).

For a 960 s spectrum, we adopt the following criteria for steady conditions: $\sigma_{\rm HC} \leqslant 0.02$ and σ_s/μ (8.6–18.0 keV) $\leqslant$ 10%. The steady 960 s spectra generally have excellent statistics for spectral modeling. We obtain 2374 such spectra in the Z stages, about 79% of the total. Almost all nonsteady intervals are on the FB.

3.4.2. Sample Intervals

We now examine several sample Z tracks from the time intervals marked in Figure 4, corresponding to MJD 53756.6–53767.3, 53870.5–53876.2, 53893.0–53898.0, 54112.0–54119.0, 54188.0–54196.5, 54268.5–54277.0, and 54290.0–54299.0, respectively. These intervals span about 5–10 days and are selected based on their small secular changes in the CDs/HIDs. Their light curves, CDs, and HIDs are shown in Figure 10; the first and second columns are the light curves and CDs, respectively, and HIDs are plotted in the third and fourth columns. The light curves have bin size 32 s as in Figure 4, but in this case the intensity is the sum of all four energy bands (2.2–18.0 keV). From the light curves, we see that the source evolves back and forth between different branches more than once in each sample interval. However, the corresponding CDs and HIDs (960 s bin size) each show only a single track. We therefore conclude that the secular changes in each sample interval are small. For the HIDs we differentiate two types of 960 s spectra. Data points from steady intervals

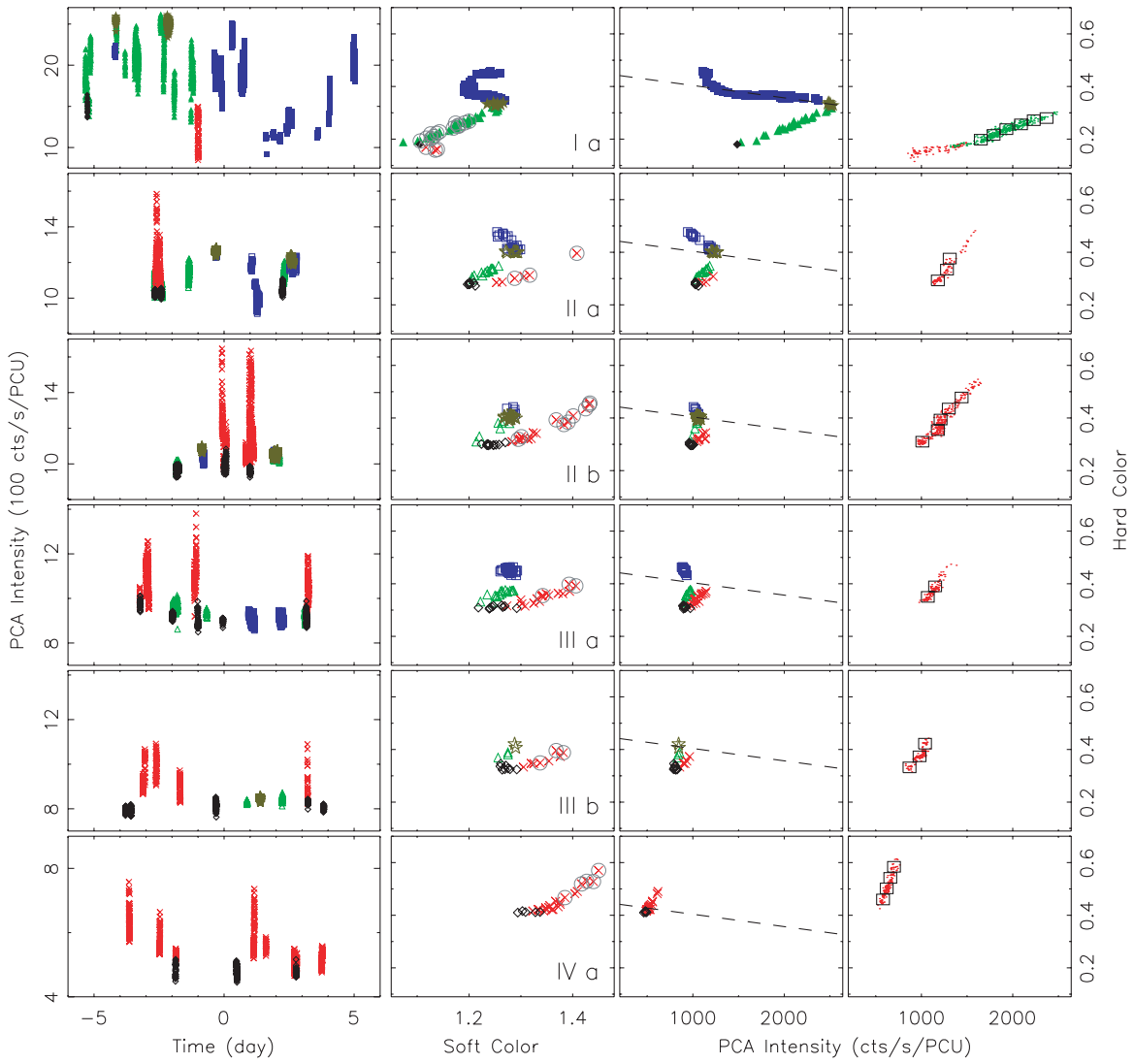

Figure 10. Light curves, CDs, and HIDs of the sample intervals marked in Figure 4. The light curves are from 32 s spectra and the CDs from ∼960 s spectra. The HIDs for the steady (Section 3) and nonsteady spectra (circled in the CDs) are shown in the third and fourth columns, respectively. The nonsteady HIDs use the 32 s subintervals, and spectra within each box shown in these HIDs are combined to form a spectrum used for spectral fitting in Section 4.3.

are plotted in the third column. The steady 960 s spectra are used for spectral fitting without further grouping. We circle the nonsteady 960 s spectra in the CDs and show their corresponding HIDs in the fourth column using their 32 s subintervals. To gain statistical precision, while avoiding spectral variability, we use boxes in the HIDs to group similar 32 s spectra and produce one spectrum per box (with exposures greater than 300 s) for spectral fitting in Section 4.

We can compare the CDs/HIDs of the sample intervals from XTE J1701−462 with those from other Z sources (Figure 1). To aid in this comparison we plot in Figure 11 the ratios of spectra from key positions along the Z tracks in these sample intervals, analogous to what is displayed in Figure 2. The blue dotted lines correspond to the ratio of the spectra at the HB/NB vertex relative to the open end of the HB, the green dashed lines show the ratio of the spectra at the HB/NB vertex relative to the NB/FB vertex, and the red dot-dashed lines show the ratio of the spectra at the outer end of the FB relative to the NB/FB vertex. The ratios are defined to divide spectra with higher PCA intensity by ones with lower PCA intensity. The comparison of Figures 10 and 11 with Figures 1 and 2 confirms that stage I is consistent with being Cyg-like, while stages II–IV are Sco-like.

Figure 11 (blue dotted lines) shows that when the source descends the HB toward the HB/NB vertex, the intensity increases at low energies, but decreases at high energies. The pivot point is ∼20 keV in interval Ia, decreasing to ∼10 keV in the later intervals. We note that the HB in the interval IIa seems to represent conditions that are still in transition from a Cyg-like to a Sco-like Z source based on such spectrum ratio. This is consistent with the fact that the HB in this interval spans a large intensity range and appears horizontal in the HID, similar to Cyg-like sources (Figures 1). The increase in the intensity as the source moves from the NB/FB vertex to the HB/NB vertex (green dashed line) reaches maximum at energies >10 keV. Moreover, in later intervals the intensity is almost constant below 7 keV. As for the FB, in interval Ia the intensity decreases as the source evolves along the FB from the NB/FB vertex, signifying a "dipping" FB (Homan et al. 2007c). This is different from the typical Cyg-like Z sources (Figures 1 and 2), where intensity initially increases from the NB/FB vertex along the

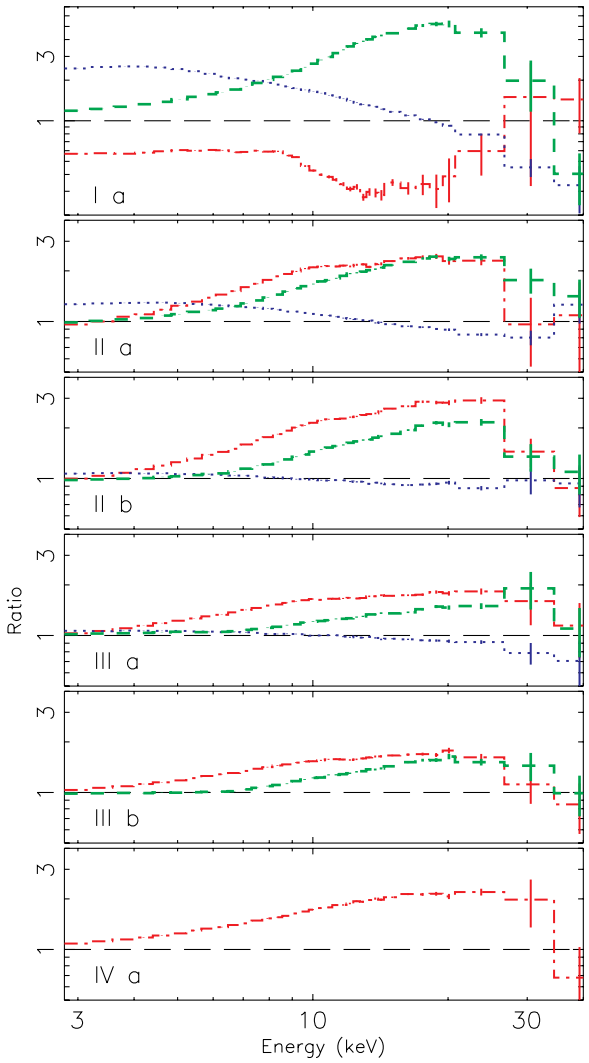

Figure 11. Comparison of the PCA spectra of XTE J1701−462 in key positions along the Z tracks from the sample intervals (Section 3.4.2). Blue dotted lines represent the ratio of the spectra at the HB/NB vertex relative to the left end of the HB. Green dashed lines show the ratio of the spectra at the HB/NB vertex relative to the NB/FB vertex. Red dot-dashed lines show the ratio of the spectra at the outer end of FB relative to the NB/FB vertex.

FB, sometimes followed by dips that appear midway along the FB. The FB of XTE J1701−462 in stage I only shows dipping. This dipping increases suddenly at energies between 10–20 keV (Figure 11), perhaps indicating some type of occultation effect. In the Sco-like stages, the FB is quite long in the CDs/HIDs and the source intensity increases when moving away from the NB/FB vertex, most obviously in the high-energy band 10–30 keV. All these details support the conclusion that stages II–IV are Sco-like.

4. SPECTRAL MODELING

4.1. Spectral Models and Assumptions

We used the hybrid model from LRH07 (Model 6) to fit the X-ray spectra of XTE J1701−462. In this model, the soft-state spectra are fit with a combination of MCD, BB, and CBPL. The CBPL component is a constrained BPL ($E_b = 20$ keV and $\Gamma_1 \leqslant 2.5$) that can assume the role of weak Comptonization. The atoll hard-state spectra are fit with a combination of BB and BPL.

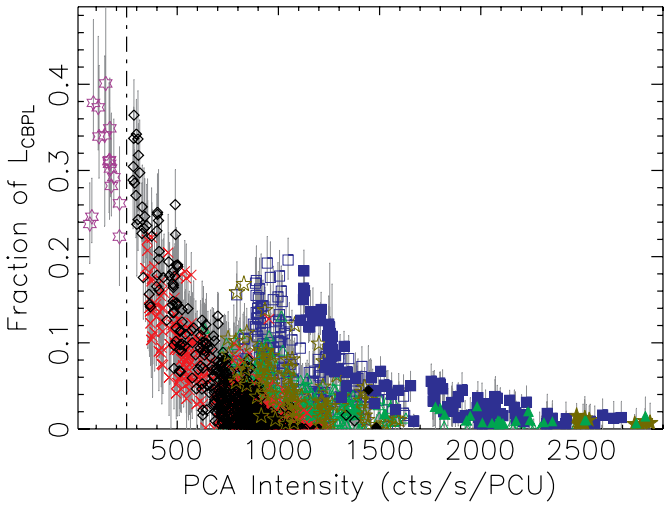

Figure 12. Fraction of the L_{CBPL} with 1σ error bars in the SS of atoll stage and in the steady spectra from all the Z stages.

As in LRH07, the PCA and HEXTE pulse-height spectra were fitted jointly, with the normalization of the HEXTE spectrum relative to the PCA spectrum allowed to float between 0.7 and 1.3 (the average best-fitting value is 0.99 ± 0.12). For the PCA spectra, we used energy channels 4–50, corresponding to 2.7–23 keV. For the HEXTE spectra, we used 20.0–80.0 keV for hard-state observations and 20.0–50.0 keV for soft-state ones. A Gaussian line was also included in the fit, with its central line energy constrained to be between 6.2–7.3 keV (the average best-fitting value is ∼6.5 keV) and the intrinsic width of the Gaussian line (σ) fixed at 0.3 keV. Interstellar absorption was taken into account with the hydrogen column density fixed at $N_H = 2.0 \times 10^{22}$ cm^{-2}. The values of the hydrogen column density and the intrinsic width of the Gaussian line were based on joined fit of simultaneous observations of this source with *Swift* and *RXTE*.

The orbital inclination of the binary system cannot be very high ($\lesssim$75), as eclipses or absorption dips were not observed in this source. However, the Fe emission line is quite weak (equivalent width $\lesssim$50 eV), compared to other Z sources (e.g., White et al. 1986; Cackett et al. 2008), and this could imply that the inclination is not very low, either (Fabian et al. 2000). In this paper, a binary inclination of 70° was assumed. The luminosity and radius-related quantities were calculated using a distance of 8.8 kpc, inferred from type I X-ray bursts that showed photospheric radius expansion (Lin et al. 2007a, 2009).

LRH07 showed that the CBPL component is only required at low-L_X soft-state observations. At higher L_X, most spectra can be fit by the MCD+BB model. In Figure 12, we show the fraction of the L_{CBPL} using steady 960 s spectra in Z stages and all spectra in the atoll SS (Section 3.4.1). The L_{CBPL} was obtained by integrating from 1.5 keV to 200 keV. The choice of the upper limit is not critical since Γ_2 is normally >2. The majority (∼91%) of the steady spectra in the Z stages have L_{CBPL} that is less than 10% of the total luminosity. There are two situations when the CBPL component contributes significantly. The first is when the source intensity is low, at the end of the Z stage and in the atoll SS. The second is when the source enters the HB in the Sco-like Z stages or the upturn of the HB in the Cyg-like Z stage (∼800–1300 counts s^{-1} PCU^{-1}; Figure 6). In the top panel of Figure 13, we show a sample spectrum with a

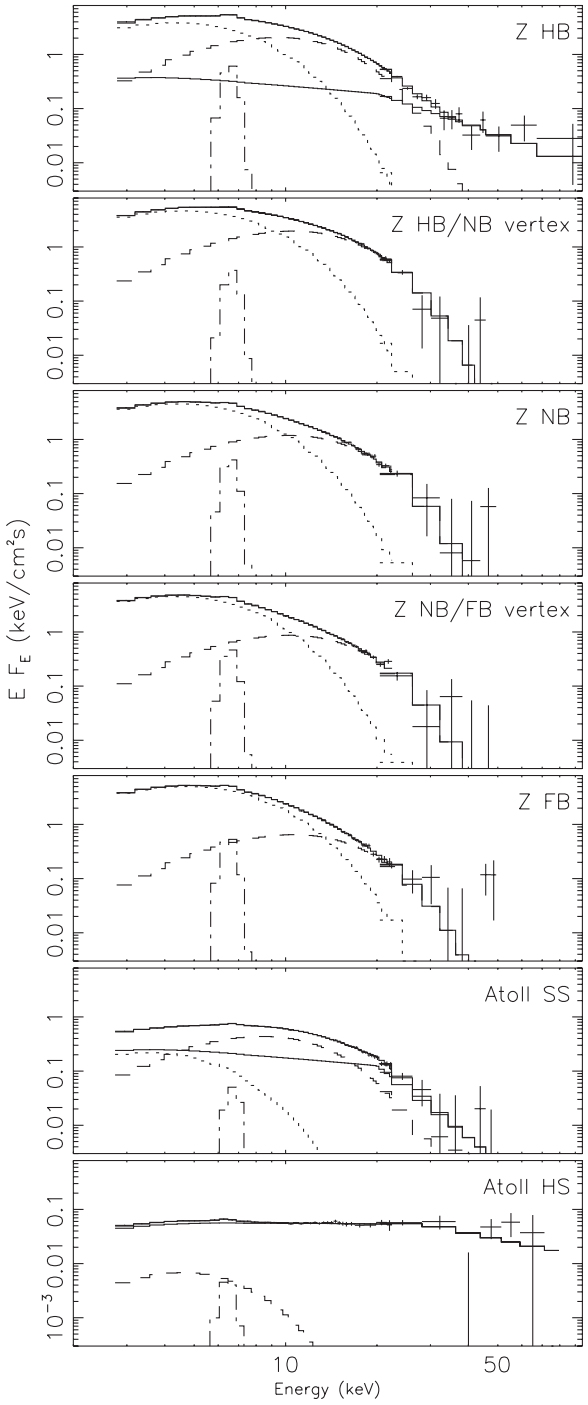

Figure 13. Examples of unfolded spectra at different states/branches. The total model fit is shown as a solid line, and it consists of an MCD component (dotted line), a BB (dashed line), a CBPL component (double-dot-dashed line), and a Gaussian line (dot-dashed line). The spectrum at the top panel shows the detection of a hard tail on the HB.

hard tail extending above 100 keV, from the upturn of the HB in sample interval Ia. It is a combination of six observations made on 2006 February 2–3, with observation IDs 91106-02-02-12 and 91106-02-03-[01–05]. The combined spectrum has an total exposure of 15 ks, a hard color of 0.39 and an intensity near 1260 counts s^{-1} PCU^{-1}.

We also fit the steady 960 s spectra in the Z stages using the MCD+BB model, i.e., without the CBPL to account for a possible hard tail. About 90% of these spectra have an increase in the total χ^2 smaller than 4.6 (compared to the MCD+BB+CBPL model), a 90% confidence level criterion for the inclusion of the CBPL in the final fit for each spectrum. The initial photon index Γ_1 often reaches the hard limit in the fit of soft spectra so that the CBPL has only two free parameters in practice.

Figure 13 illustrates the unfolded spectra in different states/branches. The spectrum at the top panel is the one that we used to show the detection of a hard tail (see above). The sample spectra corresponding to the Z-source HB/NB vertex, NB, NB/FB vertex, and FB are all from sample interval IIa, and all have exposures ∼960 s and intensities ∼1200 counts s^{-1} PCU^{-1}. There is no CBPL component in these unfolded spectra, because the inclusion of such a component does not improve the χ^2 (see above). The spectrum corresponding to the atoll-source SS is from observation 93703-01-02-11, with an exposure of 6155 s and an intensity of 181 counts s^{-1} PCU^{-1}. The spectrum corresponding to the atoll-source HS is a combination of observations 93703-01-03-14 and 93703-01-03-16, with an exposure of 13 ks and an intensity of 17 counts s^{-1} PCU^{-1}.

The spectral fit results are shown in the following sections. For clarity, we only plot data points with small error bars, i.e., if the difference between the upper and lower limits (90% confidence) of the temperature of the thermal components is smaller than 0.7 keV. In the end, 1.1% and 2.4% of the data points for the MCD and BB components are omitted, respectively.

4.2. Atoll-Source Stage

Since our spectral model was developed for observations of transient atoll sources, we begin the fitting process of XTE J1701−462 with the atoll stage (V). We compare our results with those from LRH07, to see whether the spectral evolution in stage V is consistent with the behavior of other atoll sources. The CD and HID for this stage are shown in the bottom panel of Figure 5. The spectral fits show that the fraction of the $L_{\rm CBPL}$ can reach more than 30% in the SS (Figure 12). The HS observations are very faint and are dominated by the BPL component (∼95%) with initial photon index ∼2. The spectral fit results for the MCD and BB components are shown in Figure 14.

The left panel shows the luminosity of each thermal component versus its color temperature, $kT_{\rm BB}$ or $kT_{\rm MCD}$. For reference, we also show the lines for constant radius, assuming $L_{\rm X} = 4\pi\sigma_{\rm SB}R^2T^4$. The NS radius (8 km), inferred from type I X-ray bursts for an assumed distance of 8.8 kpc (Lin et al. 2009), is shown with double-dot-dashed lines in Figure 14. The dot-dashed lines correspond to $R = 6.0$ km, and the dashed lines to $R = 1.7$ km. These latter two values are derived from the fit to the obtained best-fitting $R_{\rm MCD}$ and $R_{\rm BB}$ values, respectively. The inner disk radius is comparable with the inferred NS radius. However, we note that these values have large systematic uncertainties, since accurate measurements require knowledge of the distance, inclination, and other parameters such as the hardening factors for the disk and burst spectra.

The most remarkable result seen in Figure 14 is that the disk and boundary components evolve roughly along $L_{\rm X} \propto T^4$ tracks, consistent with LRH07 results for Aql X-1 and 4U 1608−52. Moreover, the boundary layer is small and remains nearly constant in size throughout the SS. This can be seen in the right panel of Figure 14, which shows the best-fitting $R_{\rm MCD}$ and $R_{\rm BB}$ versus the source intensity. $R_{\rm BB}$ cannot be constrained very well in the HS, but its values are marginally consistent with those from the SS.

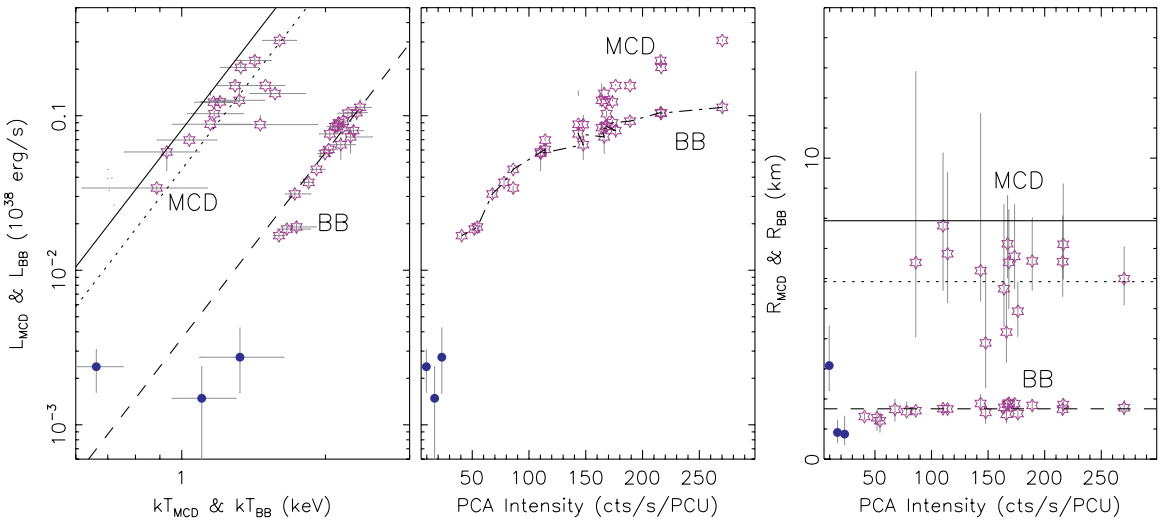

Figure 14. Spectral fitting results for the atoll stage of the outburst (stage V), using MCD+BB+CBPL for the SS and BB+BPL for the HS. There is no MCD component for the HS, and the blue filled circles correspond to the BB in all panels. The luminosities of the thermal components (MCD/BB) are plotted against their characteristic temperatures and the PCA intensity in the left and middle panels, respectively. The data points for the BB component in the SS in the middle panel are connected by a dot-dashed line for clarity. The right panel shows the characteristic emission size of the thermal component vs. the PCA intensity. The double-dot-dashed line corresponds to the size of the NS inferred from type I X-ray bursts. The dotted and dashed lines correspond to $R = 6.0$ km and $R = 1.7$ km, respectively, assuming $L_X = 4\pi R^2 \sigma_{SB} T^4$.

(A color version of this figure is available in the online journal.)

In the middle panel of Figure 14, we show the luminosity of each component (the MCD and BB) versus the PCA intensity. This plot makes it easy to link the spectral results to the HID in Figure 5. To help distinguish the two spectral components, the data points for the BB results in the SS are connected by a dot-dashed line.

4.3. Z-Source Stages

The spectral evolution in the Z stages is more complex. To understand the physical processes that drive the evolution of Z sources along different branches, we carried out spectral fits for the samples of the Z tracks that were discussed earlier (time intervals marked in Figure 4 and light curves, CDs, and HIDs shown in Figure 10). As explained in Section 3.4.2, we fit steady 960 s spectra directly, and we use box selections in the HIDs to combine 32 s spectra accumulated from the nonsteady intervals. The spectral fitting results for the sample intervals are shown in Figure 15, one row for each interval. The quantities plotted in the three panels of each row are the same as for Figure 14. The results are discussed below, one Z branch or vertex at a time.

In addition to our consideration of these sample intervals, we also fit all the steady 960 s spectra of the four Z stages. The results are shown in Figure 16 for each branch/vertex. Some spectral results for nonsteady observations in the sample intervals are also included in this figure. The dotted and dashed constant radius lines from Figure 14 are again shown in Figures 15 and 16 for reference.

4.3.1. The NB/FB Vertex

We begin the assessment of our spectral results for the Z stages by considering the evolution of the NB/FB vertex (black diamond symbols), which is globally shown to be well organized in Figure 16. When the Z-source behavior departs from the atoll track (Figure 14), the disk no longer follows the $L_{MCD} \propto T_{MCD}^4$ relationship, and R_{MCD} begins to increase with intensity.

To see this effect more clearly, we plot the radii of the thermal components versus the total L_X in units of L_{EDD} for the NB/FB vertex in Figure 17, with the results from the atoll track in stage V also included for comparison. L_{EDD} is taken to be 3.79×10^{38} erg s^{-1}. This value was estimated to be the Eddington luminosity for NS type I X-ray bursts showing photospheric radius expansion (Kuulkers et al. 2003). This value was also used to infer the distance of 8.8 kpc for XTE J1701−462 (Lin et al. 2009). We note that the same results would be obtained if we take the net flux from the spectral fit, while correcting the MCD term by inclination effect, and then divide by the average maximum flux measured for the two radius expansion bursts. Finally, we note that $L_{X,EDD}$ is a quantity that is useful for scaling purposes only, since proper considerations of the Eddington limit should consider the disk and boundary layer of Z sources separately (Section 6), and, in addition, it is likely that a portion of the BB flux is obscured by the disk (LRH07).

In Figure 17, we see that the inner disk radius remains constant, at a value presumed to represent the innermost stable circular orbit (ISCO), until L_X reaches ∼0.2 L_{EDD}. Above this luminosity, the inner disk radius increases with luminosity. This is quite possibly a signature of the local Eddington limit in the disk and will be further discussed in Section 6. When XTE J1701−462 deviates from the $L_{MCD} \propto T_{MCD}^4$ track, its evolution is consistent with $L_{MCD} \propto T_{MCD}^{-4}$, or equivalently $L_{MCD} \propto R_{MCD}$, with T_{MCD} slightly decreasing with L_{MCD}.

In contrast to the behavior of the disk radius, the boundary layer ($R_{BB} \sim 1.7$ km) maintained its small (nearly constant) size from the atoll stage to all observations in the NB/FB vertex, with luminosity ranging from ∼0.01 to 1 L_{EDD}. These results suggest an intimate relation between the atoll track and the NB/FB vertex.

4.3.2. The FB

The behavior of the FB is evaluated from the results of the sample intervals, shown in red cross symbols in Figure 15. Besides the two constant radius lines, we also plot solid lines for which $L_{MCD} \propto T_{MCD}^{4/3}$. These lines describe the relationship between disk luminosity and inner disk temperature when the

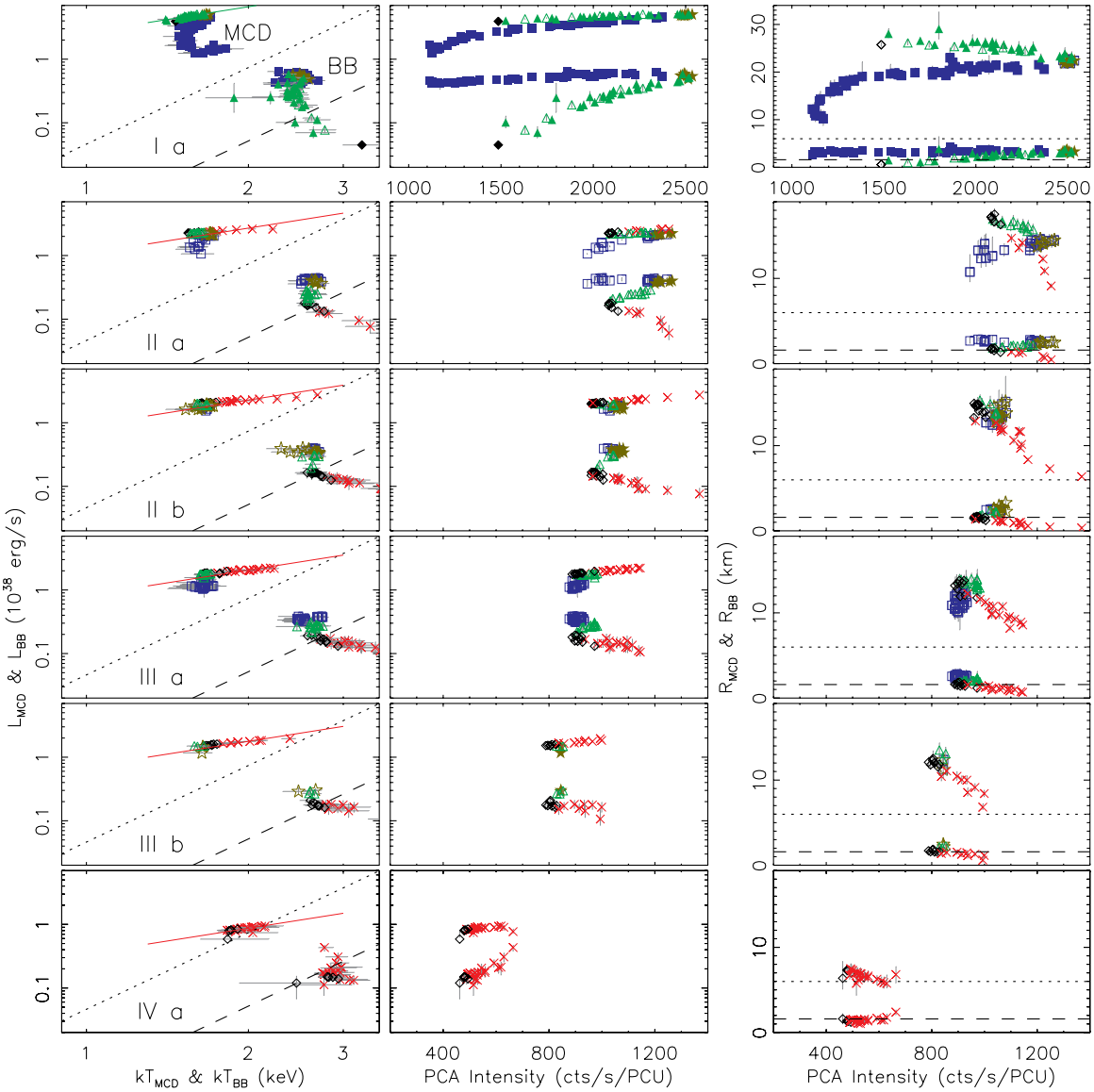

Figure 15. Spectral fitting results for the sample intervals (see Section 3.4.2). As in Figure 14, the luminosities of thermal components (MCD/BB) are shown vs. their characteristic temperatures and vs. the PCA intensity. The right column shows the characteristic emission size of the thermal component vs. the PCA intensity. Each row of panels corresponds to one sample interval. The dotted line and dashed line in Figure 14 are replotted here for reference. In each panel, results of the MCD are always at the top, and those of the BB at the bottom.

source has a variable inner disk radius at a constant accretion rate, as shown in the following. The disk temperature T at radius R is (Hayakawa 1981)

$$T(R) = \left(\frac{3GM\dot{m}}{8\pi\sigma_{SB}R^3}\right)^{1/4}, \quad (1)$$

where M is the mass of the NS. Evaluating the above equation at the inner disk radius and considering that $L_{MCD} = 4\pi\sigma_{SB}R_{MCD}^2T_{MCD}^4$ (Mitsuda et al. 1984), we obtain

$$L_{MCD} = 4\pi\sigma_{SB}\left(\frac{3GM\dot{m}}{8\pi\sigma_{SB}}\right)^{2/3}T_{MCD}^{4/3}. \quad (2)$$

A constant $\dot{m}$ then leads to $L_{MCD} \propto T_{MCD}^{4/3}$, as represented by the red solid lines in Figure 15.

This figure shows that the FB tracks closely follow the red solid lines, implying that the disk evolution is consistent with an inner disk radius varying under the condition of a constant $\dot{m}$. In the NB/FB vertex the disk is truncated at a larger radius than in the atoll stage. The FB is traced out when the disk refills temporarily and the inner radius shrinks to the value seen in the atoll stage, which is presumed to be the ISCO. As $\dot{m}$ increases, the disk in the NB/FB vertex is truncated at a progressively larger radius, thereby shifting and lengthening the constant $\dot{m}$ line along which the disk evolves on the FB. The superposition of these tracks can be seen in the left bottom panel of Figure 16.

The BB component contributes less as the source ascends the FB, especially in the intervals from stages II–III. At the same time, the temperature appears to increase, while the effective radius sharply decreases. We have no interpretation for these effects, and it is also possible that the results are affected by systematic problems with our model when one component (BB, in this case) contributes a small fraction of the flux. The FB of interval Ia is of the dipping type, and its spectra cannot be fit well by the MCD+BB+CBPL model. Therefore, the results for the FB of this interval are not shown.

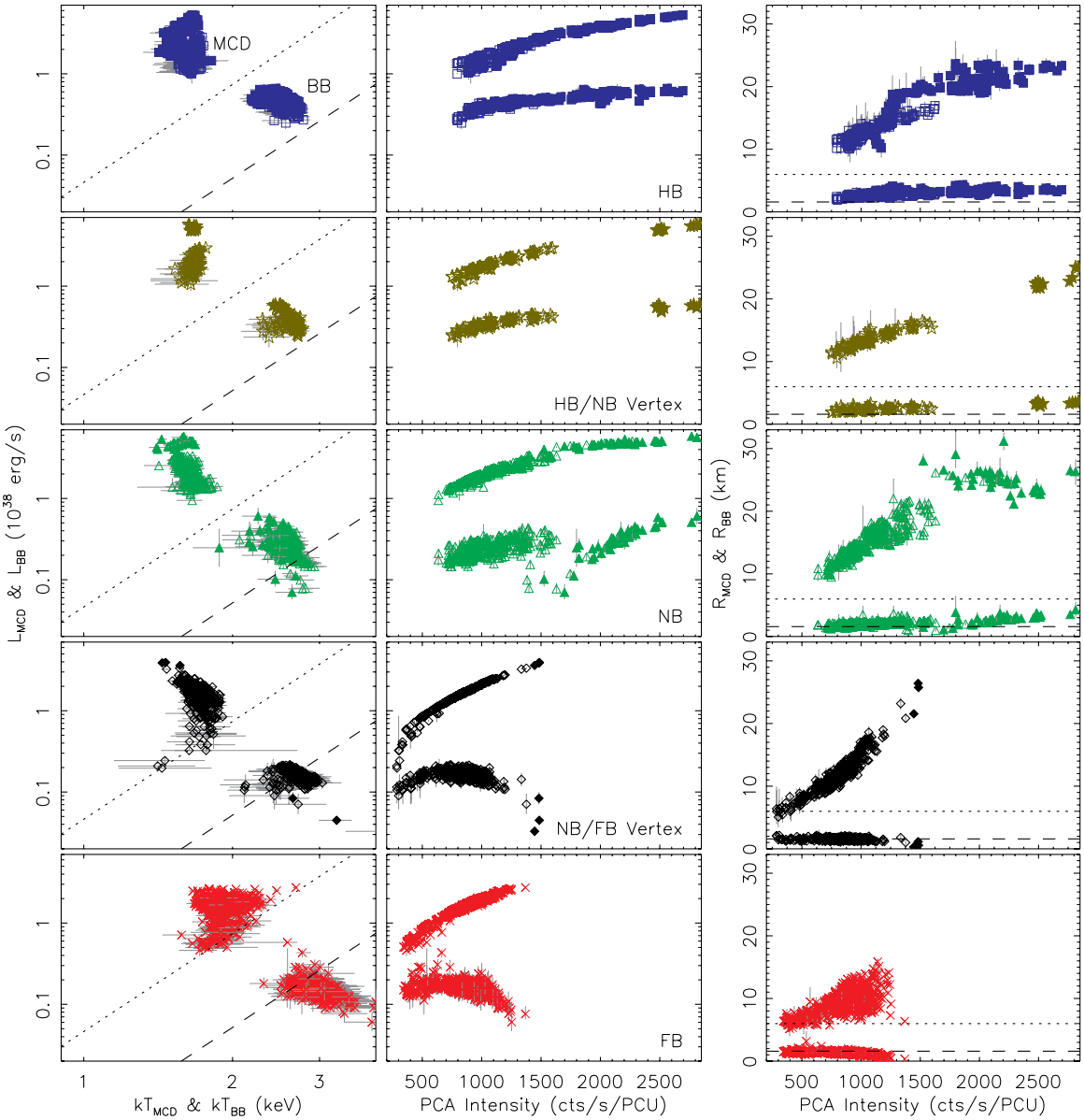

Figure 16. Same as Figure 15, but combining all observations throughout the Z stages of the outburst. From the top to the bottom, the rows correspond to the HB, HB/NB vertex, NB, NB/FB vertex, and FB, respectively. The results are derived from the steady 960 s spectra plus the spectra created from the boxes shown in Figure 10.

4.3.3. The NB

Results from the sample intervals (Figure 15) show that, as the source ascends the NB in the Sco-like stages II–III, the MCD component seems to remain unchanged, while the BB radius increases at constant temperature. The latter effect causes an increase in the source intensity at energies around 10–30 keV, with almost no change at energies <7 keV (green dashed lines in Figure 11). Since the NB is mainly the result of a changing BB radius, it is interesting to see whether the difference of the spectra from the two ends of the NB can be fit by a BB model. We test this on the NB in sample interval IIIa. Excluding the region around the Fe line near 6.4 keV, the resulting spectrum (Figure 18) can indeed be fit by a BB, with temperature $kT_{BB} = 2.71 \pm 0.03$ keV. This temperature is close to that of the individual spectra on this particular NB, confirming that the source evolution along the NB is mostly due to an increase in the normalization of the BB at constant temperature. The difference spectrum shows a dip around the Fe line, indicating that the Fe line emission is stronger at the lower part of the NB, despite the fact that the source intensity at the lower part of the NB is lower.

On the NB of interval Ia the BB still changes very significantly, but in that case there is also a clear change in the MCD parameters, roughly consistent with evolution at a constant $\dot{m}$ through the disk (Figure 15). From the NB/FB vertex toward the HB/NB vertex, L_{MCD} and kT_{MCD} increase while R_{MCD} decreases. The L_{BB} and R_{BB} also increase. All this results in a large increase in the source intensity, at energies around 10–30 keV (Figure 11).

The possible origins of the BB increase on the Sco-like NB are discussed in Section 6. The coupled changes in the MCD and BB components for the Cyg-like NB seem to be complicated, and we have no simple picture of the corresponding physical changes.

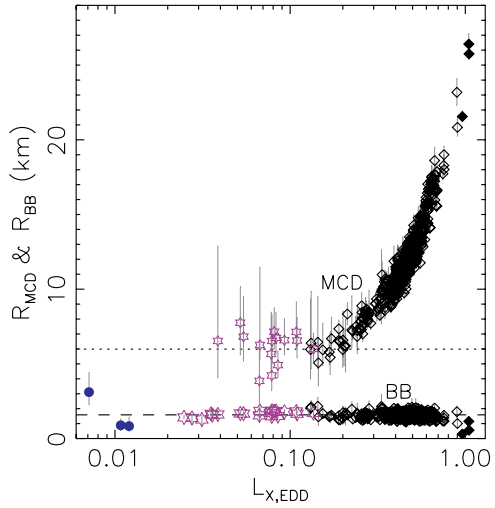

Figure 17. Emission sizes of the thermal components vs. the total L_X for the NB/FB vertex and the atoll-source stage V.

(A color version of this figure is available in the online journal.)

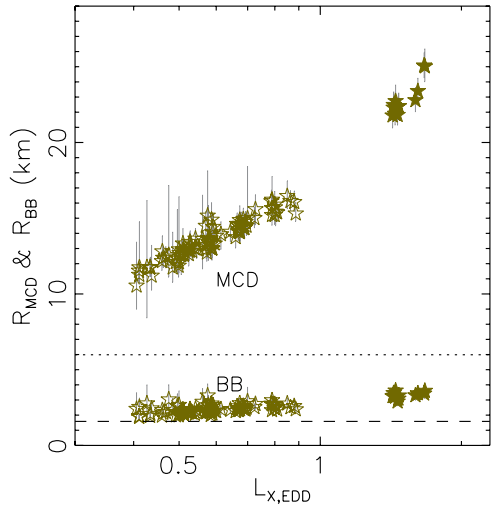

Figure 19. Emission sizes of the thermal components vs. the total L_X for the HB/NB vertex.

(A color version of this figure is available in the online journal.)

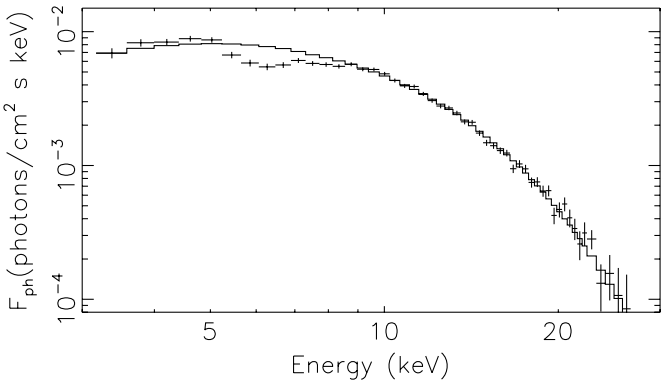

Figure 18. Difference of spectra for the two ends of the NB during interval IIIa. The spectrum is fit with a BB model (solid line) excluding the region 4.5–8 keV around the Fe line. The success of this model confirms that the evolution along the NB during this Sco-like Z stage is mostly due to the changes of the boundary layer emission area.

4.3.4. The HB/NB Vertex

Similar to the NB/FB vertex, the behavior of HB/NB vertex in the HID is well organized, i.e., it evolves along a single line in Figure 6. Since there is little change in the MCD component on the NB of the Sco-like stages, the differences between the MCD quantities of the HB/NB vertex and those of the NB/FB vertex are small (Figure 15). Only when the luminosity increases above a certain value do their differences become significant. This is reflected in the global spectral results for the HB/NB vertex in Figure 16: kT_{MCD} in the HB/NB vertex hovers around 1.6 keV, whereas kT_{MCD} in the NB/FB vertex shows a slight decrease at high luminosity.

Both R_{BB} and R_{MCD} increase with intensity. The visible BB effective radius always appears smaller than the disk radius and never reaches the values of the inner disk radius seen in the atoll stage. Both L_{MCD} and L_{BB} increase with intensity, but L_{MCD} increases much faster.

Although the Cyg-like and Sco-like Z tracks are quite different, the data points of HB/NB vertex in Cyg-like Z stage I seem to lie along the high-L_X extension of the points of the HB/NB vertex in the Sco-like Z stages II–IV. Figure 19 shows the emission sizes R_{MCD} and R_{BB} of the thermal components with respect to the total L_X, instead of the intensity. The HB/NB vertex extends from ~0.4 to 1.7 Eddington luminosity, and the R_{MCD} and R_{BB} both increase with luminosity. However, there is a gap between 0.9–1.4 L_{EDD}.

4.3.5. The HB

The HB is first investigated using the sample observations (Figure 15). In general, L_{MCD} decreases as the source ascends the HB away from the HB/NB vertex. This causes changes in the spectrum at low energies, as shown in Figure 11 (blue dotted lines). The BB component, however, varies little. In contrast with the decrease in the intensity at low energy, there is an increase in the intensity at high energies, going out along the HB. This is mostly due to an increase of the Comptonized component (Figure 12), which for the Cyg-like Z stage mostly occurs on the upturn of the HB. The significant detection of Comptonization on the HB of the Z stages is consistent with a series of discoveries of hard tails in other Z sources (Paizis et al. 2006; Farinelli et al. 2005; Di Salvo et al. 2000, 2001; D'Amico et al. 2001), although there are claims of hard tail detections on branches other than the HB in some of these reports.

To illustrate the coupled behavior between the MCD and the CBPL components on the HB more quantitatively, we plot in Figure 20 the fractions of the L_{MCD} (upper panels) and the L_{MCD} + L_{CBPL} (lower panels) for sample intervals Ia and IIIa. The results for all observations on the HB and HB/NB vertex are also plotted, on the right. We can see that while the fraction of the L_{MCD} on the HB changes by 20% (upper panels), the fraction of the L_{MCD} + L_{CBPL} maintains a much smoother track over the Sco-like Z tracks. On shorter timescales, the quantity L_{MCD} + L_{CBPL} changes also very little over a typical Sco-like HB, e.g., only 5% for interval IIIa. The above results imply that in the Sco-like Z stages, as the source climbs up the HB, thermal emission from the disk is converted into a hard component by Comptonization. This is also true for the upturn of the HB in the Cyg-like Z stage. Thus, the similarity between the Sco-like HB and the upturn of the Cyg-like HB is supported by both the fraction of Comptonization and the coupling between the MCD and CBPL luminosities.

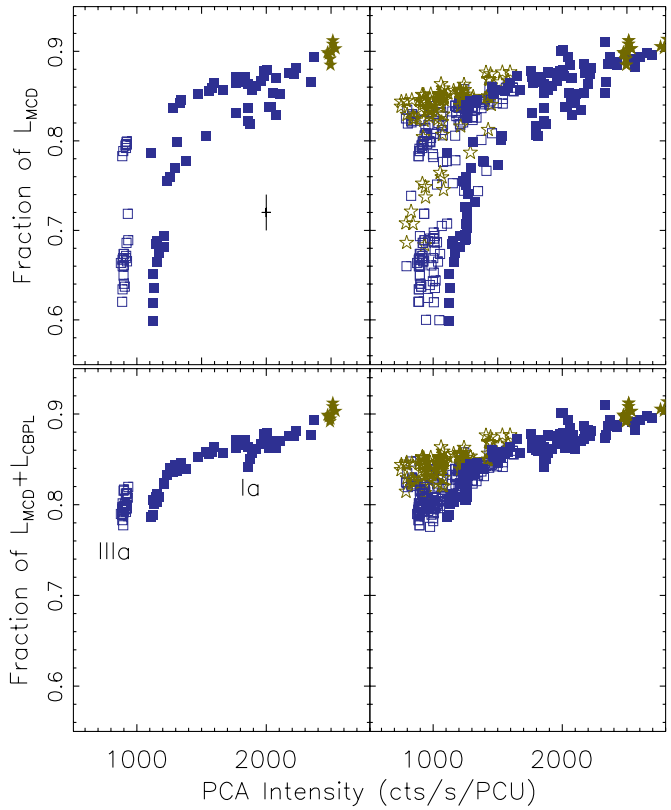

Figure 20. Fractions of the L_{MCD} (upper panels) and $L_{MCD+CBPL}$ (lower panels) on the HB and the HB/NB vertex. Left panels show sample intervals Ia and IIIa, while the right panels show the entire outburst.

(A color version of this figure is available in the online journal.)

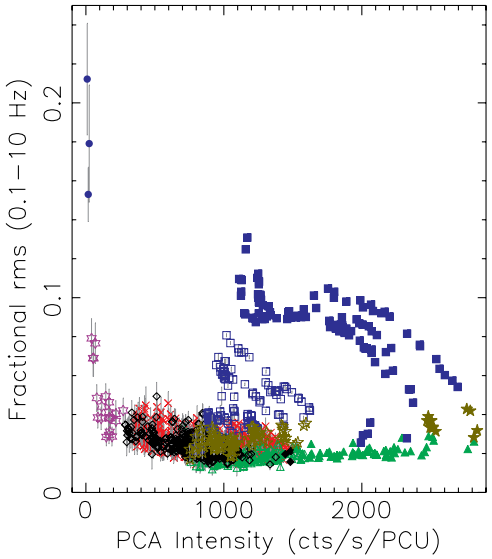

Figure 21. rms from 0.1 to 10 Hz for the entire outburst. Elevated continuum power (i.e., rms > 5%) in the PDS is limited to the Z-source HB and atoll-source HS.

(A color version of this figure is available in the online journal.)

5. BROADBAND VARIABILITY

Although this work mostly focuses on the spectral properties of XTE J1701−462, timing properties are important tools for understanding the evolution along atoll and Z tracks. In LRH07 we used a measure of the broadband variability to compare the results of our spectral fits to those obtained for black hole systems. In particular, we focused on the relation between the fraction of Comptonized flux and the strength of the variability, as measured by the integrated (fractional) rms in the power density spectrum (PDS; 0.1–10 Hz).

In Figure 21, we plot the integrated rms versus the PCA intensity for XTE J1701−462. Similar to the classical atoll sources, the power is very weak in the atoll SS (less than 6%) and increases in the atoll HS. In the Z stages, except for the HB, the power is always very weak, with typical rms of 2%. Although the Sco-like HB typically has a small intensity range (∼100 counts s^{-1} PCU^{-1}), the rms can increase quite significantly, by up to 4%, from the HB/NB vertex to the tip of the HB. We attribute this rms increase to the growing importance of Comptonization on the HB. This is consistent with the result in LRH07, in which we found that the rms is strongly tied to the fraction of the Comptonized component for both atoll sources and black hole binaries.

On the upturn of the Cyg-like HB the rms increases significantly, another aspect that makes it similar to the Sco-like HB. However, the rms on the upturn of the Cyg-like HB is higher than on the Sco-like HB. Moreover, on the nonupturn part of the Cyg-like HB, the rms already increases strongly, even though the Comptonization fraction remains low (Figure 20). The analysis of the frequency resolved spectroscopy on the typical Cyg-like Z sources (Gilfanov et al. 2003) indicated that this boost in rms seems to arise from the boundary layer.

6. DISCUSSION

6.1. Secular Evolution of XTE J1701−462 and the Role of $\dot{m}$

During its 2006–2007 outburst, XTE J1701−462 successively shows characteristics of Cyg-like Z, Sco-like Z, and atoll sources, and the stages for each source type are clearly correlated with the X-ray luminosity. The Z tracks move substantially in the HID, while creating distinct lines for the upper (HB/NB) vertex and the lower (NB/FB) vertex, respectively (Figure 6). The line for the lower vertex smoothly connects to the atoll track. XTE J1701−462 shows a large dynamic range in luminosity that is typical of X-ray transients, and the overall shape of the broad band light curve is expected to represent the temporal evolution of $\dot{m}$. It is then straightforward to examine Figure 3 and Table 1 and conclude that the transitions between source types and the secular changes in the HID are both driven by the changes in $\dot{m}$.

A more detailed accounting of $\dot{m}$ can be derived from the results of our particular X-ray spectral model, which tracks the contributions from the MCD, the BB, and weak Comptonization. We first focus on the MCD, since the disk radiation is always the strongest component in the spectrum, except for the atoll hard state, and the origin of the radiation is upstream of any effects of the Eddington limit. We can infer $\dot{m}$ from the MCD model through (Frank et al. 1985)

$$\dot{m} = \frac{2L_{\rm MCD}R_{\rm MCD}}{GM}. \quad (3)$$

Figure 16 shows that for each of the vertices, both $L_{\rm MCD}$ and $R_{\rm MCD}$ increase with intensity, implying that $\dot{m}$ changes monotonically along each of the two vertex lines. If we use $\dot{m}$ for the MCD at the upper luminosity end of the atoll stage as a reference value, then there is a factor ∼30 increase in $\dot{m}$

in the lower vertex at the upper luminosity end of the Sco-like Z stage (i.e., near 1400 counts s^{-1} PCU^{-1}), and factors ∼40 and ∼60 increase at the brightest points in the lower and upper vertices, respectively, of the Cyg-like Z stage. These ratios are larger than the corresponding ratios in luminosity or PCA intensity, because, for the same $\dot{m}$, an increasingly truncated disk produces radiation with decreasing efficiency. These accretion rates would amplify the sense in which XTE J1701−462 is seen to be an extraordinary X-ray transient.

Our spectral results for the MCD also provide insights as to how the Eddington limit might affect the behavior of Z source. In the atoll stage, $R_{\rm MCD}$ remains constant, and the value is presumably close to the radius of the ISCO. In the Z stages, $R_{\rm MCD}$ increases with $L_{\rm MCD}$ (and $\dot{m}$) along the NB/FB vertex line (Figure 17). One may interpret this result as the effect of the local Eddington limit in the disk. The Eddington limit is reached when the radiation pressure overcomes the force of gravity. For a spherical case, both gravity and radiation forces vary as r^{-2}, and the Eddington limit has a single value that covers all radii. However, in a disk system, both the gravity and radiation forces depend more complicatedly on r, and the Eddington limit should be reached locally (Katz 1980; Fukue 2004). In a standard disk (Equation (1)), the locally generated luminosity varies as r^{-3}, and radiation pressure most effectively moves matter in the vertical direction, while the vertical component of gravity force roughly varies as r^{-2}, if we assume that the thickness of the disk scales linearly with r. When $\dot{m}$ increases to a certain point, the inner disk must adjust to the radius where the local Eddington limit is reached, while at larger radii the disk can continue to produce thermal radiation (Katz 1980; Fukue 2004).

Detailed considerations of super-Eddington mass flows in accretion disks have shown $\dot{m}$ regimes in which the disk is thickened, an advective or quasi-radial accretion flow dominates the region inside the inner disk radius, and substantial mass may be driven out of the system (Katz 1980; Watarai et al. 2000; Mineshige et al. 2000; Fukue 2004; Ohsuga & Mineshige 2007). Such accretion solutions are often referred to as "slim disk" models. Structural changes for the slim disk will modify the $T(r)$ function, so that the emergent spectrum will no longer resemble the MCD model. However, the divergence between these models might not be apparent until $\dot{m}$ is much larger than the critical value that first brings the inner disk to the Eddington limit at the ISCO (Mineshige et al. 2000).

Slim disk models depend on the mass of the compact object and the accretion rate, and there are additional considerations required for effects of general relativity and of radiative transfer through the thick disk. Furthermore, such models are usually applied to accreting black holes, which are free from the additional emission from the boundary layer and its illumination of the inner disk. In black hole studies, observers look for evidence of slim disks in high-luminosity soft-state observations in which the MCD model does not fit the data well, while a more generic disk model based on the function, $T \propto r^{-p}$, constrains p to be somewhat lower than the value ($p = 0.75$) required for the MCD (Okajima et al. 2006). Application of a slim disk model for XTE J1701−462, which requires careful considerations of the NS boundary layer, is beyond the scope of this investigation. We note, however, that we do not see a χ^2 barrier for our spectral model when the source is very bright, which suggests that the deviations between the disk spectrum and the MCD model are not large in the observed bandpass (3–50 keV).

We have seen that both the upper and the lower vertices evolve along two distinct lines, respectively, in the HID over a large overlapping intensity range (Figure 6). However, the variations of the MCD and BB components along the upper vertex line are different from those along the lower vertex line (Figure 16). This might imply that the system is able to respond to the variations in accretion rates in two different ways along these two vertex lines. We have discussed two possible disk solutions above (i.e., standard thin disk vs. slim disk), and thus it is possible that the two vertices assume these two different solutions for disk accretion, respectively. This idea will be further discussed in the following section in terms of the behavior of the source along the NB, which bridges these two vertices.

Our model fits additionally track the apparent conditions in the NS boundary layer, via the spectral parameters for the BB component. At the lower vertex, it is apparent that $L_{\rm BB}$ increases much more slowly than $L_{\rm MCD}$ and even decreases at the highest intensity in the Z-source stages (Figure 16). In addition, there is no evidence for BB radius expansion during the evolution that spans the atoll stage and the lower vertex in the Z stages (Figure 17). Thus, we can find no clear evidence on the lower vertex track for any critical point at which Eddington limit is reached in the BB, which is expected to expand and evolve in spectral shape as the luminosity passes through the Eddington limit (Inogamov & Sunyaev 1999; Popham & Sunyaev 2001). This casts doubt on the idea that the gradual expansion of the disk with increasing luminosity at the lower vertex might be some type of disruption caused by the emission from boundary layer. On face value, our spectral results imply that significant mass outflow from the inner disk edge (in the Z stages) limits $L_{\rm BB}$ to levels below or near the Eddington limit at the surface of the NS.

Other investigations have looked for an Eddington signature in the behavior of the BB temperature. A value of $kT_{\rm BB}$ ∼2.4 keV was found to be a high-luminosity limit for accreting NSs that were studied with the Fourier-frequency resolved spectroscopy technique (Gilfanov et al. 2003; Revnivtsev & Gilfanov 2006). This value is close to the peak temperature seen in radius expansion bursts (Galloway et al. 2008), while a peak value ∼2.7 keV is found for two such bursts from XTE J1701−462 (Lin et al. 2009). In both Z-vertices, the NB, and the HB (Figure 16), $kT_{\rm BB}$ hovers near 2.7 keV, with a trend toward slightly lower temperature and slightly larger $R_{\rm BB}$ at highest $L_{\rm BB}$. Thus, unless there is variable obscuration of the BB region that masks more substantial changes in conditions there, we surmise that at the lower vertex the BB hovers near its Eddington limit and that the BB inherits an increasingly smaller fraction of the $\dot{m}$ that flows through the disk, as $\dot{m}$ increases.

Once the inner disk radius is set by the Eddington limit in the lower (NB/FB) vertex, the only branch that tries to reverse this condition is the FB. In the upper vertex, there is a second evolution track for secular variations in which both $R_{\rm MCD}$ and $R_{\rm BB}$ expand with increases in luminosity. It is therefore possible that the mechanism for the NB (i.e., the addition of quasi-radial flow or some other mechanism) might bring the system to super-Eddington conditions in both the disk and the boundary layer in the upper (HB/NB) vertex, while only the disk experiences such conditions in the lower vertex. Our use of the term "super-Eddington" means, respectively, disk $\dot{m}$ in excess of the Eddington limit when the inner disk radius is at the ISCO, and boundary layer $\dot{m}$ in excess of the accretion

limit at which the optical surface still coincides with the NS surface.

6.2. Physical Processes Along the Z Branches of XTE J1701−462

We have found that spectral evolution along the Sco-like FB is consistent with a shrinking of the inner disk radius, while $\dot{m}$ remains constant (Figure 15). When we combine the interpretations for the FB and the NB/FB (lower) vertex, with further consideration of the increasing evolution speed along the FB (Figure 7), we arrive at the following scenario. For a given value of $\dot{m}$, the Sco-like Z sources accrete matter through a truncated disk, with inner radius set by a local Eddington limit (not by the ISCO). The FB is an instability that springs from the NB/FB vertex, and it represents a temporary push by the inner disk toward the ISCO. The entire FB can be traced out in ∼10 minutes, but the evolution is much faster at the top than at the bottom of the FB (Figure 7). Variations at timescales of about seconds can easily be seen in the light curve at the top of the FB. Such timescales are of order the viscous timescales of the inner disk for a viscosity parameter of 0.01 (Frank et al. 1985, Equation (5.69)). For the dipping FB in the Cyg-like Z stage, limited data and poor spectral fits prevent us from deriving any conclusions about its nature.

The NB bridges the upper and lower vertices of the Z. The Sco-like NB is traced out as the result of changes in the BB emission size, while the MCD properties remain nearly constant. Similar BB changes are seen on the Cyg-like NB, but here the disk also changes, shrinking in radius at constant $\dot{m}$ similar to the changes seen for the Sco-like FB. Taken literally, an increase of $\dot{m}$ onto the boundary layer, with no observable change in $\dot{m}$ for the disk, could suggest the onset of a radial or advective flow as a secondary accretion component. This would require that the total $\dot{m}$ increases slightly (i.e., by 10% or less) as the source ascends the NB from the lower vertex. This conjecture might be of further interest toward understanding why NS radio jets begin to be seen when a Z source begins to ascend the NB, while the jets become stronger and more steady on the HB (Migliari & Fender 2006, and references below). An alternative explanation for the Sco-like NB is that $\dot{m}$ remains constant, but the measured BB area increases as the result of the geometric changes associated with the boundary layer and/or our line of sight to it. While there are probably other explanations as well, it is important to point out one important constraint: the range of the NB at a specific $\dot{m}$ is not arbitrary, as we can see from the two vertex lines (Figure 6). Moreover, the process responsible for tracing out the NB appears to be another type of instability, as the source evolves faster on the NB than in the two vertices (Section 3.3).

In Section 6.1, we pointed out that the upper and lower vertices might assume two different solutions for the disk accretion, as they evolve along two distinct lines in the HID over a large overlapping intensity range, while the best-fitting results for the two main components MCD and BB are different. In addition, the two vertices appear to be stable compared with the evolution along the NB, and the upper vertex is most often seen at higher luminosity (Figures 17 and 19). Both the standard and slim disks are possible stable accretion disk solutions at high accretion rates with the slim disk associated with higher accretion rates and an increased amount of radial advection flow (see references in Section 6.1). Also considering that the increase of the BB emission size along the NB might be explained by an additional radial flow, we hypothesize that in the upper vertex the disk assumes a slim disk solution while the disk in the lower vertex is a standard thin disk. In that case, the NB is formed as the additional radial flow turns on and the source begins the transition to the slim disk.

As demonstrated in Section 4.3.5, the Sco-like HB is traced out as the thermal emission in the disk is converted into a hard component by Comptonization, while the combined luminosity from the disk and Comptonization (i.e., $L_{\rm MCD} + L_{\rm CBPL}$) remains roughly constant. In the most variable case, which is sample IIa, the combined luminosity varies by 10% relative to the mean HB value, and we have shown that this early Sco-like HB has some lingering characteristics of the Cyg-like stage. Thus, it remains quite possible that the Sco-like HB is traced out at constant $\dot{m}$ through the disk. The Cyg-like HB consists of a long horizontal line in the HID, plus an upturn at the far end. The upturn portion exhibits an increase in Comptonization, in common with the Sco-like HB. However, the nonupturn part of the Cyg-like HB remains puzzling. Its track in the HID resembles the secular drift in the upper vertex, which might suggest that it is not a true HB track. However, the power continuum shows strongly elevated continuum power, which is a clear signature of the HB, but from that standpoint the lack of Comptonization is very surprising. Further investigations of Cyg-like HB tracks for other sources are needed. Finally, as noted above, radio emission has been detected on the HB, presumably to be due to jet formation (Fender et al. 2007; Migliari et al. 2007; Fender & Hendry 2000; Penninx et al. 1988). For the Sco-like HB and the upturn portion of the Cyg-like HB, the association of increased Comptonization with radio flux follows a general convention for X-ray binaries. However, while the spectrum in the atoll HS is dominated by Comptonization, only modest Comptonization fractions are found for the HB in Z sources.

Given the variations in $R_{\rm MCD}$ along the FB and the Comptonization on the HB, we must use the value of $(R_{\rm MCD} \times (L_{\rm MCD} + L_{\rm CBPL}))$ to trace $\dot{m}$ through the disk for Z sources. Our overall conclusion is that for Sco-like Z tracks, $\dot{m}$ remains constant to the level of 10% or less (see also Homan et al. 2002). The role of $\dot{m}$ in the evolution along the Z tracks has been in debate for decades (Section 1). In our analyses, what distinguishes the Z branches is not $\dot{m}$ but the different mechanisms that spring from the Z vertices, which are the more stable reference points along the Z track. The three branches are associated with different forms of spectral evolution, and our physical interpretations are different from the concept that Z track evolution is driven by changes in any single parameter.

Unstable nuclear burning was invoked as a mechanism for the FB by Church et al. (2008), using observations of Cyg-like Z sources. In their scenario, there are no changes in $\dot{m}$. We cannot determine whether this explanation works for the Cyg-like dipping FB of XTE J1701−462, but it clearly does not work for the FB in the Sco-like stages. We note that one type I X-ray burst has been observed in an FB during its decay back to the NB/FB vertex (Lin et al. 2009). We further test this explanation on stage IV as follows. For a solar abundance, the ratio of the nuclear and gravitational energies is only about 2.5% (Strohmayer & Bildsten 2006). However, the Sco-like FB is frequent (Table 1), and the luminosity variations are very strong. We calculate the net flaring fluence on the FB in stage IV by subtracting the associated lower vertex flux from each FB flux measurement and integrating over time, and the nonflaring fluence is simply the total fluence minus the flaring fluence. Their ratio turns out to be very high, ∼33% for stage IV.

6.3. Comparison with Other NS LMXBs

Stage I was shown to be very similar to the typical Cyg-like Z sources, especially GX 5−1 and GX 340+0, by Homan et al. (2007c) based on the CDs/HIDs and variability. The major difference is in the FB. Cyg X-2 is similar to XTE J1701−462 in that it also has substantial secular changes and sometimes even changes between source types (Kuulkers et al. 1996; Wijnands et al. 1997). A more detailed comparison between these two sources could be valuable.

In Sco-like stages II–III, XTE J1701−462 is very similar to the Sco-like Z sources. The color and spectral similarities between XTE J1701−462 and the typical Sco-like Z sources, shown in Figures 2 and 11, imply that the spectral fitting results for XTE J1701−462 should also apply to the Sco-like Z sources.

In stage IV, the HB and NB are no longer observed, and the CDs/HIDs resemble those of the bright persistent GX atoll sources GX 9+1, GX 9+9, and GX 3+1. These sources are believed to accrete at accretion rates between those of the classical atoll sources (such as Aql X-1 and 4U 1608−52) and those of the Z sources (Hasinger & van der Klis 1989; van der Klis 2006). Based on patterns traced out in the CDs, they are very similar to XTE J1701−462 in the Z stage IV. We classify such patterns in the CD/HID for XTE J1701−462 into the NB/FB vertex and the FB, while the bright persistent atoll sources have typical names "lower banana" and "upper banana," respectively (Hasinger & van der Klis 1989; van der Klis 2006). It is possible that the lower banana in the GX atoll sources is simply the NB/FB vertex and the upper banana is the FB. This can be investigated with spectral fits, e.g., to see whether the upper banana shows evidence for typical FB spectral evolution, as shown in Figure 15.

In the brief atoll stage, XTE J1701−462 resembles the classical transient atoll sources Aql X-1 and 4U 1608−52 from the CDs/HIDs and spectral fits (LRH07). The emission size of the boundary layer remains constant across the states, and the inner disk radius remains constant in the SS. The increase of the Comptonization in the HS is also accompanied by an increase in continuum power, i.e., the integrated rms in the PDS. We also note that XTE J1701−462 in the atoll stage has a peak luminosity of $\sim$0.2 $L_{\rm EDD}$, while Aql X-1 and 4U 1608−52 show maxima of $\sim$0.35 $L_{\rm EDD}$ (LRH07). We note that these values are scaling estimates only, as there might be large corrections required to infer intrinsic emission for some components, e.g., the BB which might be partially obscured.

7. CONCLUSIONS

Our results offer a major departure from the classical view of Z sources. The Sco-like Z track is traced out at nearly constant $\dot{m}$, while the three branches are tied to different physical mechanisms that function like instabilities tied to the more stable Z vertices. On the other hand, the secular changes, which are driven by variations in $\dot{m}$, unite, in sequence, all of the subclasses of atoll and Z sources.

The conclusions 3–6 below are primarily derived from our chosen spectral model, especially from the MCD component. The behavior of the BB component is more difficult to understand, as this component might be significantly affected by mass loss, obscuration, etc. We acknowledge the need to test this model on the persistent Z sources to determine whether such conclusions can be generalized. We also acknowledge the need to further consider systematic problems associated with the model and with the literal interpretation of physical quantities derived from the spectral parameters. Finally, there are alternative spectral models that convey different physical interpretations for the mechanisms of Z branches (e.g., Church et al. 2008), and detailed comparisons are required for these models and their associated predictions.

1. In the nearly-20-month-long outburst in 2006–2007, XTE J1701−462 evolves through the characteristic behaviors of the Cyg-like Z, Sco-like Z, and atoll sources as its luminosity decreases from super-Eddington values toward quiescence. Our spectral fits suggest that as $\dot{m}$ decreases NS LMXBs change from Cyg-like Z, via Sco-like Z, to atoll sources.
2. As the $\dot{m}$ decreases, the HB disappears first, followed by the NB, and finally by the FB. Despite the substantial secular changes during the outburst, the HB/NB and NB/FB vertices trace out two distinct lines in the HID. With the disappearance of the FB, the NB/FB vertex smoothly evolves into the atoll track traced out at the lowest accretion rate, beginning at $L_{\rm X} \sim 0.2\ L_{\rm EDD}$. The full length of the NB shortens with the decrease in luminosity.
3. In the atoll SS, the disk maintains a constant inner radius, at a value presumed to match the ISCO, and the spectral evolution follows $L_{\rm MCD} \propto T_{\rm MCD}^4$. Deviations from this behavior, in the form of increasing $R_{\rm MCD}$ with $\dot{m}$, are found in the NB/FB (lower) vertex during the Z-source stages. The truncated disk at larger radius is attributed to the effect of reaching the local Eddington limit at the inner disk radius.
4. The Sco-like FB is traced out when the disk shrinks back toward the atoll stage value at constant $\dot{m}$. This appears to be an instability in which the disk temporarily moves to reverse the truncation level set by the NB/FB vertex. The Cyg-like FB, which is of the "dipping" type in this source, cannot be satisfactorily fit with our spectral model, and its nature is unknown.
5. As the source evolves along the NB from the upper to lower vertices, the main spectral variation is the apparent size of the BB emission. This might be due to additional matter supplied to the boundary layer via the onset of a radial flow. Alternatively, there might be geometric effects that alter our view of the boundary layer while the source transverses the NB at constant $\dot{m}$. The NB seems to represent another type of instability in Z sources, since spectral evolution is faster on the NB than in its two connecting vertices.
6. The Sco-like HB is traced out when some of the energy in the disk is converted into a hard X-ray component, presumably via Comptonization, while the disk $\dot{m}$ remains roughly constant. Increasing continuum power in the PDS is also detected. The Cyg-like HB is much longer than the Sco-like one. Its upturn resembles the Sco-like HB in intensity range, strong Comptonization, and continuum power. Thus, the upturn of the Cyg-like HB probably has the same nature as the Sco-like HB. The nonupturn part of the Cyg-like HB lies along the same line traced by the HB/NB vertex in the HID. Only weak Comptonization is detected, but there is also strong continuum power, making this particular portion of the Cyg-like HB to appear unique and puzzling.
7. Finally, we speculate as to how these results can tie into theoretical investigations of accretion disks at high luminosity. Like the lower vertex, the upper vertex appears to be a more stable source condition than the Z branches. The upper vertex is more commonly seen when the source is at the highest levels of luminosity, and it is associated with an increased efficiency in the disk for passing matter

through to the boundary layer. These same properties distinguish the slim disk model from the standard thin disk. We therefore hypothesize that the two vertices coincide with the two disk models and that evolution up the NB represents the transition to the slim disk. The HB association with a stronger jet can then be interpreted as an apparent requirement that the slim disk be in place before the jet is able to attain higher luminosity, which is coupled to the appearance of increased Comptonization.

This research has made use of data obtained from the High Energy Astrophysics Science Archive Research Center (HEASARC), provided by NASA's Goddard Space Flight Center.

REFERENCES

Agrawal, V. K., & Sreekumar, P. 2003, MNRAS, 346, 933
Barret, D., & Olive, J.-F. 2002, ApJ, 576, 391
Bradt, H. V., Rothschild, R. E., & Swank, J. H. 1993, A&AS, 97, 355
Cackett, E. M., et al. 2008, ApJ, 677, 1233
Church, M. J., Jackson, N. K., & Balucinska-Church, M. 2008, Chin. J. Astron. Astrophys. Supp., 8, 191
D'Aí, A., et al. 2007, ApJ, 667, 411
D'Amico, F., Heindl, W. A., Rothschild, R. E., & Gruber, D. E. 2001, ApJ, 547, L147
Di Salvo, T., et al. 2000, ApJ, 544, L119
Di Salvo, T., et al. 2001, ApJ, 554, 49
Di Salvo, T., et al. 2002, A&A, 386, 535
Done, C., Życki, P. T., & Smith, D. A. 2002, MNRAS, 331, 453
Fabian, A. C., Iwasawa, K., Reynolds, C. S., & Young, A. J. 2000, PASP, 112, 1145
Farinelli, R., et al. 2005, A&A, 434, 25
Fender, R. P., & Hendry, M. A. 2000, MNRAS, 317, 1
Fender, R. P., et al. 2007, MNRAS, 380, L25
Frank, J., King, A. R., & Raine, D. J. 1985, Accretion Power in Astrophysics (Cambridge: Cambridge Univ. Press), 283 p
Fukue, J. 2004, PASJ, 56, 569
Galloway, D. K., Muno, M. P., Hartman, J. M., Psaltis, D., & Chakrabarty, D. 2008, ApJS, 179, 360
Gierliński, M., & Done, C. 2002, MNRAS, 331, L47
Gilfanov, M., Revnivtsev, M., & Molkov, S. 2003, A&A, 410, 217
Hasinger, G., & van der Klis, M. 1989, A&A, 225, 79
Hasinger, G., van der Klis, M., Ebisawa, K., Dotani, T., & Mitsuda, K. 1990, A&A, 235, 131
Hayakawa, S. 1981, PASP, 33, 365
Homan, J., et al. 2002, ApJ, 568, 878
Homan, J., Wijnands, R., Altamirano, D., & Belloni, T. 2007a, Astron. Tel., 1165
Homan, J., et al. 2007b, Astron. Tel., 1144, 1
Homan, J., et al. 2007c, ApJ, 656, 420
Inogamov, N. A., & Sunyaev, R. A. 1999, Astron. Lett., 25, 269
Jahoda, K., et al. 1996, in Proc. SPIE 2808 EUV, X-Ray, and Gamma-Ray Instrumentation for Astronomy VII, ed. O. H. Siegmund & M. A. Gummin (Bellingham, WA: SPIE), 59
Katz, J. I. 1980, ApJ, 236, L127
Kuulkers, E., van der Klis, M., & Vaughan, B. A. 1996, A&A, 311, 197
Kuulkers, E., et al. 1994, A&A, 289, 795
Kuulkers, E., et al. 2003, A&A, 399, 663
Levine, A. M., et al. 1996, ApJ, 469, L33
Lin, D., Homan, J., Remillard, R., & Wijnands, R. 2007a, Astron. Tel., 1183
Lin, D., Remillard, R. A., & Homan, J. 2007b, ApJ, 667, 1073
Lin, D., et al. 2009, ApJ, submitted (arXiv:0904.2187)
Migliari, S., & Fender, R. P. 2006, MNRAS, 366, 79
Migliari, S., et al. 2007, ApJ, 671, 706
Mineshige, S., Kawaguchi, T., Takeuchi, M., & Hayashida, K. 2000, PASJ, 52, 499
Mitsuda, K., et al. 1984, PASJ, 36, 741
Muno, M. P., Remillard, R. A., & Chakrabarty, D. 2002, ApJ, 568, L35
Ohsuga, K., & Mineshige, S. 2007, ApJ, 670, 1283
Okajima, T., Ebisawa, K., & Kawaguchi, T. 2006, ApJ, 652, L105
Paizis, A., et al. 2006, A&A, 459, 187
Penninx, W., Lewin, W. H. G., Zijlstra, A. A., Mitsuda, K., & van Paradijs, J. 1988, Nature, 336, 146
Popham, R., & Sunyaev, R. 2001, ApJ, 547, 355
Reig, P., van Straaten, S., & van der Klis, M. 2004, ApJ, 602, 918
Remillard, R. A., & Lin, D., The ASM Team at MIT and NASA/GSFC 2006, Astron. Tel., 696
Revnivtsev, M. G., & Gilfanov, M. R. 2006, A&A, 453, 253
Rothschild, R. E., et al. 1998, ApJ, 496, 538
Strohmayer, T., & Bildsten, L. 2006, in Compact Stellar X-ray Sources, ed. W. Lewin & M. vander Klis (Cambridge: Cambridge Univ. Press), 113
van derKlis, M. 2006, in Compact Stellar X-ray Sources, ed. W. Lewin & M. van der Klis (Cambridge: Cambridge Univ. Press), 39
van Straaten, S., van der Klis, M., & Méndez, M. 2003, ApJ, 596, 1155
Vrtilek, S. D., et al. 1990, A&A, 235, 162
Watarai, K.-y., Fukue, J., Takeuchi, M., & Mineshige, S. 2000, PASJ, 52, 133
White, N. E., et al. 1986, MNRAS, 218, 129
Wijnands, R. A. D., van der Klis, M., Kuulkers, E., Asai, K., & Hasinger, G. 1997, A&A, 323, 399